



TAMPEREEN TEKNILLINEN YLIOPISTO
TAMPERE UNIVERSITY OF TECHNOLOGY

Julkaisu 819 • Publication 819

Xiaoxue Zhang

Nanocrystalline Functional Alumina and Boehmite Materials: Synthesis, Characterization and Applications



Tampereen teknillinen yliopisto. Julkaisu 819
Tampere University of Technology. Publication 819

Xiaoxue Zhang

Nanocrystalline Functional Alumina and Boehmite Materials: Synthesis, Characterization and Applications

Thesis for the degree of Doctor of Technology to be presented with due permission for public examination and criticism in Konetalo Building, Auditorium K1702, at Tampere University of Technology, on the 21st of August 2009, at 12 noon.

Tampereen teknillinen yliopisto - Tampere University of Technology
Tampere 2009

ISBN 978-952-15-2184-3 (printed)
ISBN 978-952-15-2204-8 (PDF)
ISSN 1459-2045

PREFACE

The work presented in the dissertation was mainly carried out in the Department of Materials Science at Tampere University of Technology, Finland during the period of 2005-2008. This work was fulfilled under the supervision of Professor Tapio Mäntylä, to whom I would like to address my deepest gratitude. Without his guidance and support, this work cannot be done.

Besides, I would like to acknowledge whole-heartedly to the co-authors in my publications for their valuable contributions. Also I am grateful to all the colleagues who worked and are working in the Laboratory of Ceramic Materials especially to Dr. Erkki Levänen, Dr. Jarkko Leivo, M.Sc Juha-Pekka Nikkanen and M.Sc Mika Harju for all the scientific comments, discussions and encouragements. Furthermore, I thank deeply to all the staff members who worked and are working at the Department of Materials Science for creating such a pleasant working atmosphere. With them, I get chance and courage to practice my Finnish. All the Finnish words and phrases that I have learned from them in the daily coffee break are beneficial.

The financial supports from the Finnish Funding Agency for Technology and Innovations (Tekes), the Finnish National Graduate School on New Materials and Processes (NGS-NMP), the Finnish Foundation of Technology (TES), the City of Tampere and the Chinese government award for outstanding self-financed students abroad are gratefully acknowledged. Especially due to the financial support from NGS-NMP, I have the chance to concentrate on one research topic for 4 years, go deeper and deeper to finally accomplish my doctoral dissertation, participate in different conferences to see and to be seen, and carry out networking nationally and internationally.

Meanwhile, I wish to express my significant thanks to all the board members, supervisors and students in NGS-NMP. It has been a great pleasure to carry out the research work under their supervision, challenge, encouragement, support and company. All the frustrating, exciting and moving moments inside NGS-NMP are long-lasting memories and life-time treasures.

Moreover, I appreciate to the Chinese community in Tampere. Due to them, culture traditions are followed, home-sickness is eased, and even the days in the long dark winter become colorful.

Last but not the least, I would like to thank to all my family members especially to my parents, my parents-in-law and my husband Zhengyu Chen for their caring and

commitments, and for what they have done for me in all these years. To love and to be loved is my greatest happiness. Due to them, I feel confident, happy, satisfied, creative and passionate. They are always with me whenever I am near or far, right or wrong, happy or sad, rational or crazy. With love, I dedicate this dissertation to them. May they be blessed.

Tampere, May 2009

Xiaoxue Zhang

张晓雪

I truly believe we should never give up our hopes and dreams. The path may be rocky and twisted, but the world is waiting for that special contribution each of us was born to make. What it takes is the courage to follow those whispers of wisdom that guide us from inside. When I listen to that, I expect nothing less than a miracle.

– Marilyn Johnson Kondwani

Effort only releases its reward after a person refuses to quit.

– Napoleon Hill

(Taken from the book Chicken Soup for the Soul at Work)

Nanocrystalline Functional Alumina and Boehmite Materials: Synthesis, Characterization and Applications

ABSTRACT

In this dissertation, synthesis, characterization and applications of nanocrystalline functional alumina (Al_2O_3) and boehmite ($\gamma\text{-AlOOH}$) materials have been systematically studied. The processing method was focused on sol-gel method. The purpose was to synthesize, characterize and then find suitable applications such as superhydrophobic and antireflective applications to the as-prepared nanocrystalline alumina and boehmite materials.

Based on a modified sol-gel process, nanocrystalline flaky boehmite powder was synthesized, and transition alumina powders with morphologies of nanoparticles and nanorods with high surface areas were prepared from the flaky boehmite powder.

Furthermore, nanocrystalline α -alumina powder with novel morphology was also obtained from the flaky boehmite powder at a relatively low temperature of 1000 °C without using seed. The α -alumina crystallites of 5 nm in size were observed for the first time, and more interestingly such nanocrystallites existed on the surface of the nanorods with widths of about 15 nm and lengths of 50-300 nm. The detailed processing parameters of such nanocrystalline α -alumina powder were studied and the formation scheme of the novel morphology of such nanocrystalline α -alumina powder was illustrated, while the phase transformation from θ - to α -alumina was tentatively discussed.

More work was done to synthesize nanocrystalline α -alumina powder with nearly spherical morphology from gel powder, as compared to the nanocrystalline α -alumina powder obtained from the flaky boehmite powder.

On the other hand, flaky boehmite film was produced by spin coating from the same sol suspension as in the alumina powder processing. By modifying the surface chemistry, the boehmite film became superhydrophobic and antireflective. The formation process and thermal stability of such superhydrophobic antireflective boehmite film were studied and discussed. A set of roughness parameters was related to the superhydrophobic and the antireflective properties.

TABLE OF CONTENTS

PREFACE	i
ABSTRACT	iii
TABLE OF CONTENTS	iv
LIST OF PUBLICATIONS	vi
AUTHOR'S CONTRIBUTION	viii
LIST OF SYMBOLS AND ABBREVIATIONS	ix
1. INTRODUCTION	1
1.1 Nanocrystalline Functional Materials	1
1.2 Aims of the Study	1
1.3 Outline of the Dissertation	3
2. BACKGROUND	5
2.1 Alumina and Boehmite Materials	5
2.1.1 Alumina Polymorphs	5
2.1.2 Aluminium Hydroxides	5
2.1.3 Thermal Decomposition of Aluminium Hydroxides	5
2.1.4 Processing of Nanocrystalline Boehmite	7
2.1.5 Processing of Nanocrystalline α -Alumina	8
2.2 Sol-Gel Method	9
2.2.1 Sol-Gel Method in Short	10
2.2.2 Sol-Gel Processing of Nanocrystalline α -Alumina Powder	12
2.2.3 Nanocrystalline Boehmite Film by Boiling Water Treating the Gel Film	12
2.3 Superhydrophobic and Antireflective Applications	13
2.3.1 Superhydrophobic Self-Cleaning Surface	13
2.3.2 Superhydrophobic Antireflective Surface	15
2.3.3 Processing of Superhydrophobic Surface	17
2.3.4 Challenges of the Artificial Superhydrophobic Surface	17
3. MATERIALS AND METHODS	18
3.1 Materials	19
3.2 Experimental	19
3.2.1 Sol Suspensions	19
3.2.2 Gel Powder and Flaky Boehmite Powder	20
3.2.3 Calcinations of the Gel Powder and the Flaky Boehmite Powder	20
3.2.4 Spin Coating	20
3.2.5 Substrates	20
3.2.5 Formation of Nanocrystalline Flaky Boehmite Film	20
3.2.6 Modification of Surface Chemistry	20
3.3 Characterization Methods	21

3.3.1 X-Ray Diffraction (XRD)	21
3.3.2 Field Emission Scanning Electron Microscopy (FESEM).....	21
3.3.3 Transmission Electron Microscopy (TEM) and Selective Area Electron Diffraction (SAED)	21
3.3.4 High Resolution Transmission Electron Microscopy (HRTEM)	21
3.3.5 Gas Adsorption/Desorption Test.....	22
3.3.6 Thermogravimetry-Differential Scanning Calorimetry (TG-DSC).....	22
3.3.7 Atomic Force Microscopy (AFM)	22
3.3.8 Contact Angle Measurement	22
3.3.9 Ultraviolet-Visible Spectrophotometry (UV-Vis Spectrophotometry)	23
3.3.10 Optical Profilometry	23
4. RESULTS AND DISCUSSION	24
4.1 Nanocrystalline Transition Alumina Nanoparticles and Nanorods	24
4.2 Nanocrystalline α -Alumina at 1000 °C from Flaky Boehmite Powder.....	30
4.2.1 Morphology Analysis	30
4.2.2 Porosity Analysis.....	33
4.2.3 Formation Scheme of the Morphology of the Nanocrystalline α -Alumina.....	35
4.2.4 Phase Transformation of θ to α -Alumina.....	36
4.3 Nanocrystalline α -Alumina at 1000 °C from Gel Powder.....	37
4.4 Superhydrophobic Flaky Boehmite Film on Stainless Steel.....	39
4.4.1 Effect of Heat-Treating Gel Film on the Formation of the Flaky Structure of Boehmite.....	40
4.4.2 Thermal Stability of the Flaky Surface Structure.....	43
4.5 Superhydrophobic Antireflective Boehmite Film on Glass.....	46
5. CONCLUDING REMARKS AND SUGGESTIONS FOR FUTURE WORK	50
REFERENCES.....	53
ABSTRACTS OF THE PUBLICATIONS I-VII.....	59

LIST OF PUBLICATIONS

- I **Xiaoxue Zhang**, Mari Honkanen, Erkki Levänen and Tapio Mäntylä, Transition Alumina Nanoparticles and Nanorods from Boehmite Nanoflakes, *Journal of Crystal Growth* **310**, 2008, 3674-3679
- II **Xiaoxue Zhang**, Yanling Ge, Simo-Pekka Hannula, Erkki Levänen and Tapio Mäntylä, Nanocrystalline α -Alumina with Novel Morphology at 1000 °C, *Journal of Materials Chemistry* **18**, 2008, 2423-2425
- III **Xiaoxue Zhang**, Yanling Ge, Simo-Pekka Hannula, Erkki Levänen and Tapio Mäntylä, Process Study on the Formation of Nanocrystalline α -Alumina with Novel Morphology at 1000 °C, *Journal of Materials Chemistry* **19**, 2009, 1915-1922
- IV **Xiaoxue Zhang**, Yanling Ge, Simo-Pekka Hannula, Erkki Levänen and Tapio Mäntylä, Formation of Nanocrystalline α -Alumina in Different Morphology from Gel Powder and Boehmite Powder: a Comparative Study, *Ceramic Transactions*, accepted for publication
- V **Xiaoxue Zhang**, Mari Honkanen, Viljami Pore, Erkki Levänen and Tapio Mäntylä, Effect of Heat Treating Gel Films on the Formation of Superhydrophobic Boehmite Flaky Structures on Austenitic Stainless Steel, *Ceramics International* **35**, 2009, 1559-1564
- VI **Xiaoxue Zhang**, Mari Honkanen, Mikael Järn, Jouko Peltonen, Viljami Pore, Erkki Levänen and Tapio Mäntylä, Thermal Stability of the Structural Features in the Superhydrophobic Boehmite Films on Austenitic Stainless Steels, *Applied Surface Science* **254**, 2008, 5129-5133
- VII **Xiaoxue Zhang**, Mikael Järn, Jouko Peltonen, Viljami Pore, Tommi Vuorinen, Erkki Levänen and Tapio Mäntylä, Analysis of Roughness Parameters to Specify Superhydrophobic Antireflective Boehmite Films Made by the Sol-Gel Process, *Journal of the European Ceramic Society* **28**, 2008, 2177-2181

Other publications on the research area but not included in the dissertation:

- VIII **Xiaoxue Zhang**, Viljami Pore, Mikael Järn, Jouko Peltonen, Tommi Vuorinen, Erkki Levänen and Tapio Mäntylä, Effect of Temperature and Film Thickness on the Antireflective Property of Superhydrophobic Boehmite Films Made by the Sol-Gel Technique, *Proceedings of the 10th International Conference of the European Ceramic Society*, Berlin, Germany, June 17-21, 2007, 1407-1412
- IX **Xiaoxue Zhang**, Mari Honkanen, Yanling Ge, Simo-Pekka Hannula, Erkki Levänen and Tapio Mäntylä, Nanocrystalline γ -Alumina and α -Alumina from Boehmite Nanoflakes, *Global Roadmap for Ceramics: the 2nd International Ceramic Congress proceedings*, Verona, Italy, June 29-July 4, 2008, 6 pages

- X **Xiaoxue Zhang**, Erkki Levänen and Tapio Mäntylä, Superhydrophobic Antireflective Boehmite Film Made by Sol-Gel Technique on Glass, *Proceedings of the Glass Performance Days 2009*, Tampere, Finland, June 12-15, 2009
- XI **Xiaoxue Zhang**, Juha-Pekka Nikkanen, Tomi Kanerva, Erkki Levänen and Tapio Mäntylä, Comparison Study of Iron Oxide Doped Alumina-Based Catalysts via Sol-Gel Technique and Liquid Flame Spray (LFS) Method on the Growth of Carbon Nanotubes (CNTs) by Decomposition of Methane, submitted to *the 11th International Conference of the European Ceramic Society*, Krakow, Poland, June 21-25, 2009

AUTHOR'S CONTRIBUTION

The author played a major role in designing and realizing the experiments, characterizing the samples, analyzing the results, writing the manuscripts, submitting the manuscripts, doing revisions and correcting proofs.

Besides the author's contribution, the manuscripts of the publications were commented by all the co-authors. The TEM testing was done by M.Sc Mari Honkanen to obtain the TEM images and the SAED patterns in publications I, V and VI. The steel disks with central holes were also made by her in publications V and VI. The HRTEM characterization in publications II-IV was done by Dr. Yanling Ge, who also helped to analyze the HRTEM results and took the FESEM images in publication II. The FESEM measurement of other samples was carried out by M.Sc Viljami Pore in publications V-VII. The TG-DSC testing was operated by Dr. Elina Huttunen-Saarivirta in publication IV. The UV-Vis spectrophotometry characterization was done by Dr. Tommi Vuorinen in publication VII. The AFM testing was operated by M.Sc Mikael Järn, who also did the writing concerning the roughness parameters analysis in publication VII.

LIST OF SYMBOLS AND ABBREVIATIONS

d_{BET}	Particle size estimated from BET surface area
d_{XRD}	Crystallite size estimated by Scherrer equation from XRD pattern
f_1	Fraction of solid material in contact with liquid
f_2	Fraction of air in contact with liquid
K	Constant in Scherrer equation
L	Liquid
n_0	Refractive index of environmental medium
n_f	Refractive index of film
n_s	Refractive index of substrate
P	Pressure
P_0	Standard pressure (usually the saturation pressure)
P_d	Palladium
P_t	Platinum
r	Ratio of the actual area of a rough surface to the geometric projected 2-dimensional area
S	Solid in page 14
S	BET surface area in page 22
S_{dq}	Root-mean-square value of surface slope
S_{dr}	Surface area ratio parameter
S_q	Root-mean-square roughness
S_{sc}	Mean summit curvature
S_{sk}	Surface skewness
t_f	Film thickness
V	Vapor
γ_{LV}	Surface tension (i.e. energy per unit surface area) between liquid phase and vapor phase
γ_{SL}	Surface tension between solid phase and liquid phase
γ_{SV}	Surface tension between solid phase and vapor phase
θ	Contact angle in page 14
θ	Diffraction angle, also called Bragg angle in page 21
θ_A	Apparent contact angle
θ_Y	Young's contact angle
λ	Wavelength
μl	Microliter
ρ	Density

α -Al(OH) ₃	Bayerite
α -AlOOH	Diaspore
γ -Al(OH) ₃	Gibbsite
AlF ₃	Aluminium trifluoride
Al(OH) ₃	Nordstrandite
Al ₂ O ₃	Alumina
AFM	Atomic force microscopy
AISI	American iron and steel institute
Al(O-sec-Bu) ₃	Aluminium tri-sec-butoxide
ALD	Atomic layer deposition
AR	Antireflective
BET	Brunauer-Emmett-Teller equation
BJH	Barett-Joyner-Halenda model
CA	Contact angle
CAS	Chemical abstracts service
CF ₃ (CF ₂) ₇ CH ₂ - CH ₂ Si(OCH ₃) ₃	(Heptadecafluoro-1,1,2,2-tetrahydrodecyl)trimethoxysilane
CNT	Carbon nanotubes
CVD	Chemical vapor deposition
C ₃ H ₇ OH	Isopropyl alcohol
C ₆ H ₁₀ O ₃	Ethyl acetoacetate
C ₁₂ H ₂₇ AlO ₃	Aluminium tri-sec-butoxide
EAcAc	Ethyl acetoacetate
FAS	(Heptadecafluoro-1,1,2,2-tetrahydrodecyl)trimethoxysilane
fcc	Face-centered cubic
FESEM	Field emission scanning electron microscopy
Fe ₂ O ₃	Iron oxide
FFT	Fast Fourier transform
FWHM	Full width at the half maximum
hcp	Hexagonal close-packed
HRTEM	High resolution transmission electron microscopy
i-PrOH	Isopropyl alcohol
JCPDS	Joint committee on powder diffraction standards
MEMS	Microelectromechanical systems
nm	Nanometer
P/P ₀	Relative pressure
RT	Room temperature
rpm	Revolutions per minute
SAED	Selected area electron diffraction
SEM	Scanning electron microscopy

SiC	Silicon carbide
STP	Standard temperature pressure
TEM	Transmission electron microscopy
TG-DSC	Thermogravimetry-differential scanning calorimetry
UV-Vis	Ultraviolet-visible
XRD	X-ray diffraction
ZnF ₂	Zinc fluoride

1. INTRODUCTION

As an essential part of our daily life, new functional materials have significant impact on the current hot issues of energy, health, food, water, communication and environment. New materials with improved functionality are consistently welcomed to the human society; meanwhile materials with more than one degree of functionality (multi-functionality) could provide more applications and opportunities of commercial success.

1.1 Nanocrystalline Functional Materials

Nanotechnology provides a tool to create new functional materials. Nano means one billionth. Measurement at this level is in nanometers (nm) – billionths of a meter. The scale that ranges from a human down to one hydrogen atom is illustrated in figure 1. Nanotechnology involves research and technology development in the range of 1-100 nm, nanotechnology creates and uses structures that have novel properties due to their small sizes, and nanotechnology builds on the ability to control or manipulate at an atomic scale [1].

Nanocrystalline materials refer to the materials for example in the forms of thin films, nanoparticles, nanotubes, nanowires with at least one dimension of less than 100 nm. There are two different processing approaches in the field of nanotechnology: the top-down and the bottom-up. The top-down process is to start with a bulk material and then break it into smaller pieces, for example carve nanoscale objects out lithographically from a substrate [2]. The top-down is focused on the technologies mainly used in electronic devices. The bottom-up approach concerns the possibility to build up the nanoscale objects via chemical reactions starting from nanometric units, for example molecular-scale precursors. This approach is closely correlated with molecules, complexes, particles, clusters, aggregates, etc [3]. The bottom-up approach consists of for example chemical vapor deposition (CVD) [4], atomic layer deposition (ALD) [5], sol-gel technique [6], self-assembly [7], aerosol-based process [8], supercritical fluid synthesis [9] etc.

1.2 Aims of the Study

By standing at the interface of materials science and chemistry, the aim was to develop a simple process to produce nanocrystalline functional alumina (Al_2O_3) and boehmite ($\gamma\text{-AlOOH}$) materials in the forms of powder and thin film, characterize them and find suitable applications. By producing nanocrystalline powder, the end product may have improved catalytic, electrical, optical and mechanical properties. Meanwhile, the morphology of the powder material is also important since it could also affect the mechanical property of the

end product, and different morphologies are required for different advanced engineering and structural applications. Finally, by combining surface chemistry to the specific nano/micro structure of the surface (nano/micro patterning), the author targeted to produce nanostructured superhydrophobic antireflective boehmite films on the substrates of stainless steel and glass.

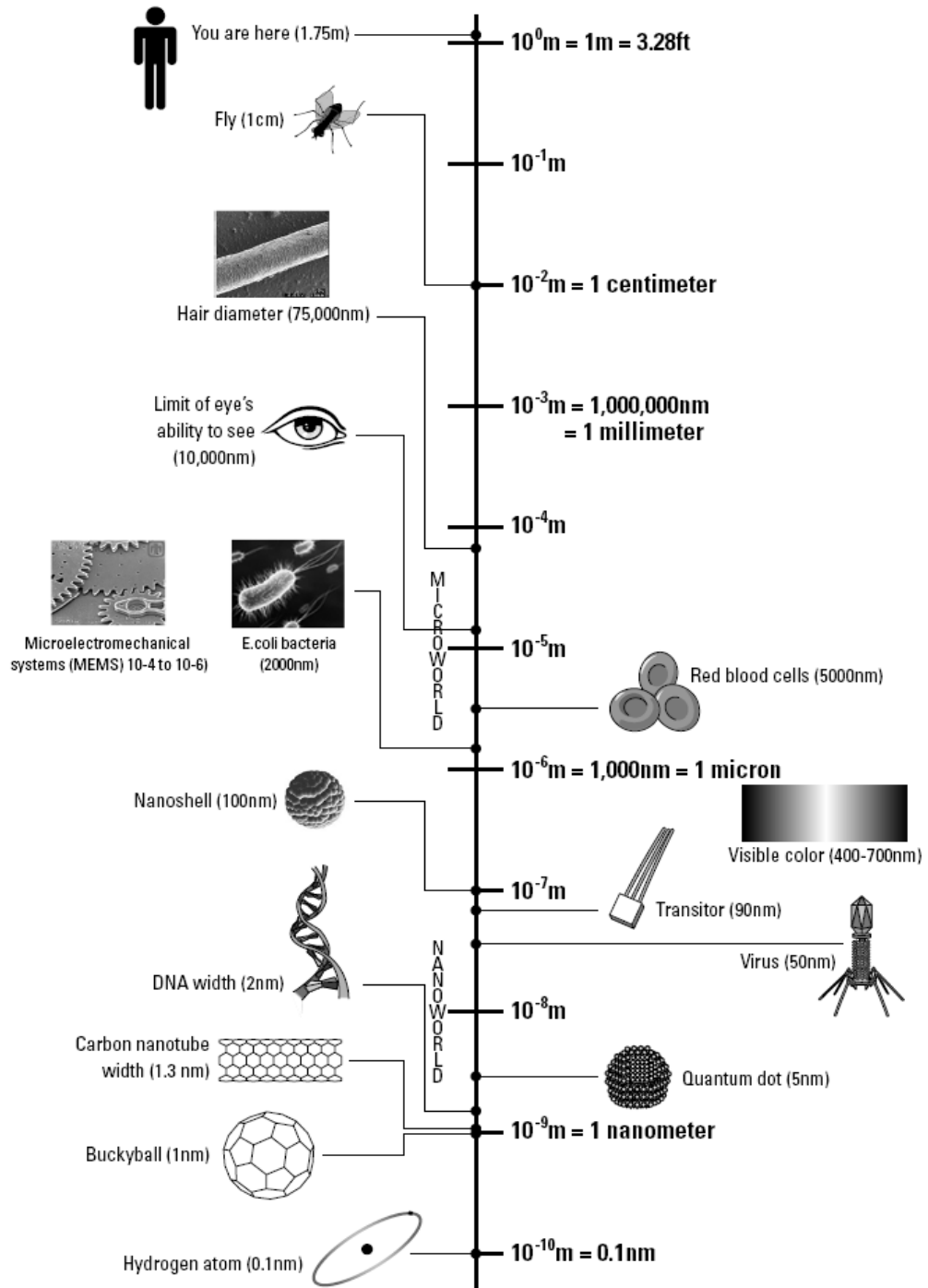


Figure 1 Illustration of the scale that ranges from a human down to one hydrogen atom [1].

1.3 Outline of the Dissertation

The dissertation is a summary of 7 peer-reviewed publications in different scientific journals and a book. The author synthesized and characterized nanocrystalline alumina powders (powder processing in publications I-IV) and superhydrophobic antireflective boehmite films (film processing in publications V-VII) based on a similar preparation process. The flow chart in figure 2 shows the processing procedures and the testing methods in each publication as well as the inter-links between the 7 publications.

Publication I studies the synthesis and characterization of the nanocrystalline transition alumina powders with high surface areas in morphologies of nanorods and nanoparticles. Publications II and III report the synthesis, characterization and formation mechanism of the nanocrystalline α -alumina powder with novel morphology obtained at a relatively low temperature of 1000 °C. Publication II is a short communication and publication III is the follow-up full paper. Publication IV compares the nanocrystalline α -alumina powder in different morphology obtained from amorphous gel powder and flaky boehmite powder. Publications V and VI report the formation process and the thermal stability of the superhydrophobic flaky boehmite film on austenitic stainless steel, and publication VII relates a set of roughness parameters to the superhydrophobic and antireflective properties of the flaky boehmite film on glass.

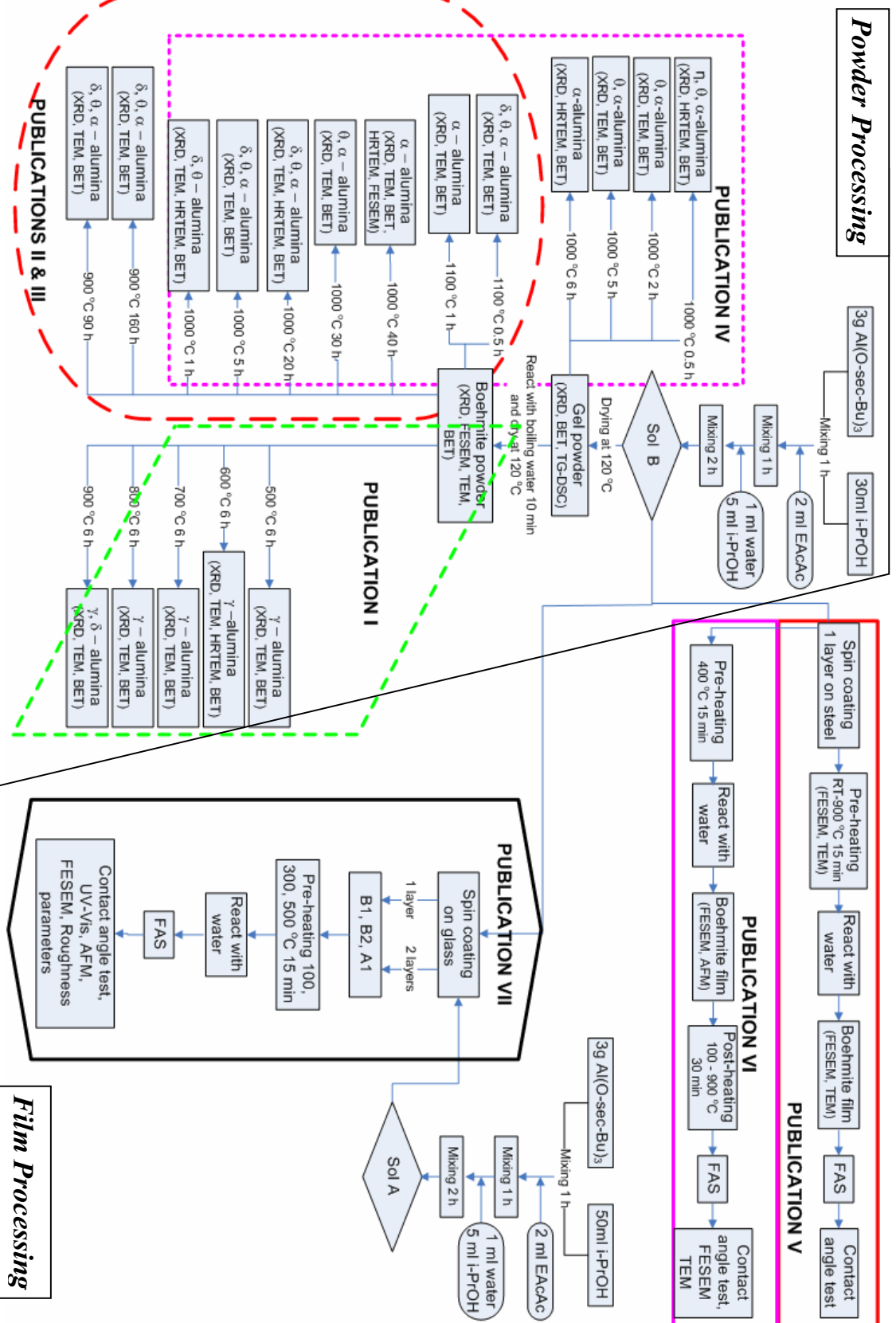


Figure 2 Flow chart of the experimental procedures, testing methods and inter-links between the results in the publications.

2. BACKGROUND

2.1 Alumina and Boehmite Materials

Alumina (aluminium oxide, Al_2O_3), in various forms, has been intimately involved in our daily life. It is present in toothpaste, porcelain bathtubs, spark plugs, tires, in the catalytic converters of our cars, and in the microchips of our TV and mobiles, etc. Meanwhile, boehmite ($\gamma\text{-AlOOH}$) is one type of aluminium hydroxides. It is an industrially important precursor for aluminas used in the manufacture of catalysts and adsorbents [10].

2.1.1 Alumina Polymorphs

The alumina structures can be divided into two broad categories based on a face-centered cubic (fcc) and a hexagonal close-packed (hcp) arrangement of oxygen anions. The distribution of cations within each subgroup results in many different alumina polymorphs. The aluminas having the fcc arrangement of oxygen anions include γ -, η -, δ - and θ -alumina; while the aluminas having the hcp arrangement of oxygen anions consist of κ -, χ - and α -alumina [11]. As the only stable polymorph, α -alumina has a high melting point, high thermal stability, high chemical inertness and high hardness. Other alumina polymorphs, also called transition aluminas, are metastable. Due to the fine particle size, high surface area and catalytic activity of their surface, transition aluminas (especially γ -alumina) find wide applications in industry as adsorbents, catalysts or catalyst carriers, coatings and soft abrasives. Meanwhile, α -alumina, as one of the most important ceramic materials, has been widely used in many applications in machine components, microelectronics, refractories, optics and lasers based on its mechanical, electrical and optical properties [12].

2.1.2 Aluminium Hydroxides

Aluminium hydroxides are typical starting materials to produce transition aluminas and α -alumina by calcining. There are two crystalline forms of aluminium monohydroxides: diaspore ($\alpha\text{-AlOOH}$) and boehmite ($\gamma\text{-AlOOH}$); and three crystalline forms of aluminium trihydroxides: bayerite ($\alpha\text{-Al(OH)}_3$), gibbsite ($\gamma\text{-Al(OH)}_3$) and nordstrandite (Al(OH)_3). An ideal structure of boehmite is shown in figure 3. The AlOOH polymeric layers are parallel to the a, c plane. These layers are stacked along the b axis and held together by hydrogen bonds between the OH groups.

2.1.3 Thermal Decomposition of Aluminium Hydroxides

The sequence of the alumina phases during the thermal decomposition of different aluminium hydroxides and gel is described in figure 4. The structure of the starting aluminium hydroxide determines the sequence of the alumina phases and the temperature range of their existence, which are different for gibbsite, bayerite, boehmite, diaspore and

gel. Depending on the processing methods, the temperature range of the alumina phases may vary.

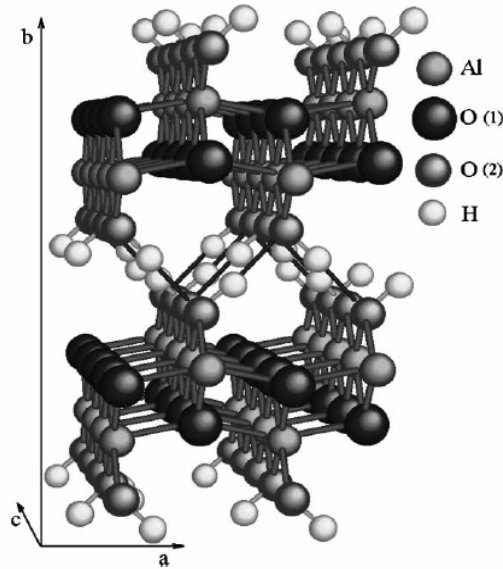


Figure 3 Ideal structure of boehmite [13].

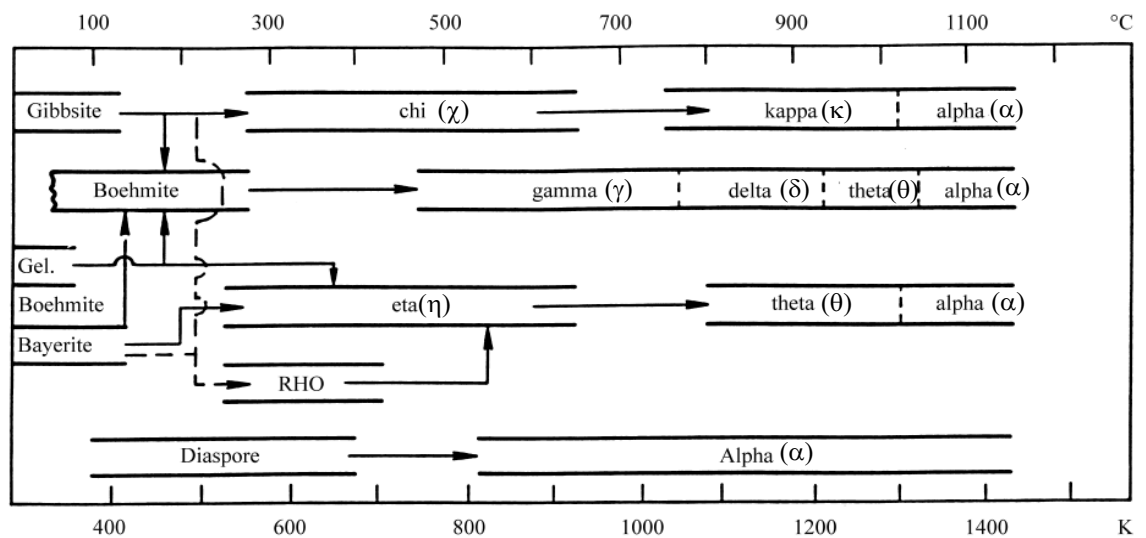


Figure 4 Sequence of the alumina phases during the thermal decomposition of different aluminium hydroxides and gel [10].

As shown in figure 4, diaspore is the only starting material which directly transforms to α -alumina without developing any intermediate transition aluminas. Due to the similarity of the diaspore and α -alumina lattices, the transformation from diaspore to α -alumina requires relatively small rearrangements and thus small nucleation energy, resulting in the formation of α -alumina at low temperatures starting from about 500 °C [10]. However, other aluminium hydroxides and gel will first transform to transition aluminas and finally to α -

alumina. The phase transformation from θ - to α -alumina involves a change in the arrangement of oxygen anions from fcc to hcp, and is generally completed at about 1200 °C [14].

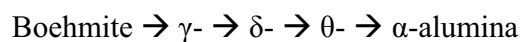
The formation of η -alumina can be confused with γ -alumina. As stated, η - and γ -alumina are both based on the fcc arrangement of oxygen anions, and table 1 gives the X-ray diffraction data of η - and γ -alumina. From table 1, it can be seen that the d value of 1.21 Å is characteristic for η -alumina. However, the diffraction peak of η -alumina with the d value of 1.21 Å only has a relative intensity of 10. If η -alumina is well crystallized and has all the diffraction peaks present in the XRD pattern, it is possible to determine the η -alumina phase. However, for nanocrystalline η - and γ -alumina, only few diffraction peaks with high degree of broadness are present in their XRD patterns. Therefore it is very difficult to distinguish nanocrystalline η - from γ -alumina. In this dissertation, nanocrystalline aluminas were studied. The author was not able to make the difference between nanocrystalline η - and γ -alumina by XRD and SAED. The discussion was based on the phase transformation sequence shown in figure 4, i.e. η - alumina was formed when gel was the starting material, and γ -alumina was obtained when boehmite was the starting material, though they had quite same XRD and SAED patterns.

Table 1 X-ray diffraction data of η - and γ -alumina [15].

η -alumina			γ -alumina		
d (Å)	I/I ₁	hkl	d (Å)	I/I ₁	hkl
4.60	40	111	4.560	40	111
2.80	20	220	2.800	20	220
2.40	60	311	2.390	80	311
2.27	30	222	2.280	50	222
1.97	80	400	1.997	100	400
1.52	20	333	1.520	30	511
1.40	100	440	1.395	100	440
1.21	10	533	1.140	20	444
1.14	20	444	1.027	10	731
1.03	10	553	0.989	10	800
			0.884	10	840
			0.806	20	844

2.1.4 Processing of Nanocrystalline Boehmite

Boehmite (γ -AlOOH) is a usual starting material to prepare γ -, δ -, θ - and α -alumina by calcining. As shown in figure 4, it passes through the following phase transformation series upon calcining:



Boehmite of different particle sizes with different morphologies from different processing methods would play important roles on the resulting aluminas obtained by calcining. Therefore different processing methods have been widely studied to produce nanocrystalline boehmite and further γ -alumina with different morphologies [16-23].

The AlOOH polymeric layers are the building blocks of the boehmite structure, as shown in figure 3. Therefore, lath-shaped boehmite crystals are frequently observed, but other morphologies can also occur, based on different processing methods and conditions. Kuiry *et al.* [16] obtained nanocrystalline fibrous boehmite powder by a modified sol-gel process involving an aluminium isopropoxide precursor. Thiruchitrambalam *et al.* [17] synthesized fibrous boehmite powder by boiling water hydrolysis of high purity aluminum metal. Liu *et al.* [18] applied hydrothermal method to produce nanocrystalline boehmite with a flower-like morphology at 160 °C. Gan *et al.* [19] reported the formation of nanocrystalline boehmite powder in different morphologies via solvothermal method at 190 °C without using template. By manipulating the volume ratio and the composition of the reaction solvents such as toluene, isopropanol and water, boehmite with morphologies of nanotubes, nanofibers, nanorods, nanolaths and nanosheets were obtained. Buchold and Feldmann [20] obtained nanocrystalline hollow boehmite spheres from a water-in-oil microemulsion by applying the liquid-to-liquid phase boundary of the micellar system as a template. Other methods include steam-assisted solid wet-gel process [21], laser ablation [22], precipitation/digestion method [23] etc.

2.1.5 Processing of Nanocrystalline α -Alumina

Diaspore would be a good starting material to produce nanocrystalline α -alumina at low temperatures, since it transforms directly to α -alumina as mentioned beforehand. However synthesis of diaspore is not easy, which requires high temperature and high pressure [10, 24-25]. Livage [26] reported a hydrothermal synthesis of diaspore at 400 °C, however boehmite can be obtained at moderate temperatures even at room temperature [16-18]. Therefore there is a continuous interest in developing processes to obtain α -alumina at relatively low temperatures from other starting materials, for example boehmite.

It is challenging to synthesize nanocrystalline α -alumina by calcining, since the complete phase transformation from θ - to α -alumina requires high temperature of about 1200 °C [14]. The high temperature calcining will result in exaggerated crystallite growth before the phase transformation to α -alumina is complete, and the formation of a vermicular structure. Wen and Yen [27] reported that as the phase transformation proceeded, α -alumina first nucleated in the fine-grained θ -alumina matrix, accompanied by particle coarsening. Then, α -alumina crystallites grew rapidly to form large colonies. Thus a network of pore channels and α -alumina "dendrites" were formed, resulting in the vermicular structure, as shown in

figure 5. The vermicular structure makes sintering to full density very difficult due to the formation of large pores that are often entrapped within the crystallites of α -alumina [28].

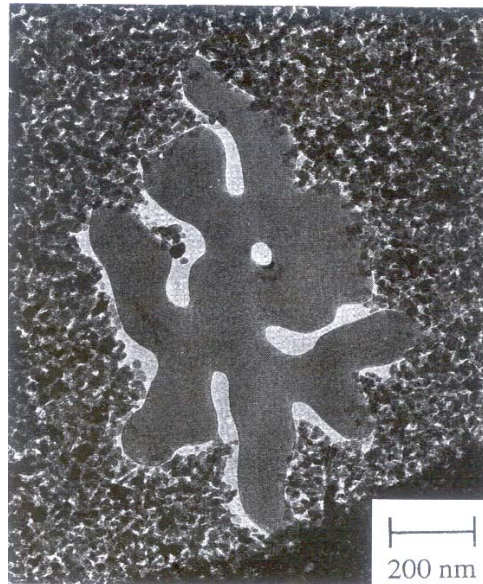


Figure 5 Image of an α -alumina colony growing into a fine-grained θ -alumina matrix [28].

A lot of effort has been addressed to find out the mechanism of the phase transformation from θ - to α -alumina [29-32]. A lot of work has also been done to find suitable seeding materials to provide heterogeneous nucleation sites for α -alumina in order to lower the formation temperature of α -alumina. Messing *et al.* firstly reported to add fine α -alumina [33] in 1984 and later α -Fe₂O₃ [30] as seeds in a sol-gel process. After that, seeding materials such as AlF₃ [34] and alumina sol [14] were also reported.

Meanwhile, spherical and plate-shaped morphologies of α -alumina have been commonly reported [35-40]. However, nanocrystalline α -alumina in different morphology would be needed for different advanced engineering and structural applications, for example nanocrystalline spherical and plate-shaped α -alumina leads to improved fracture strength and toughness in the end product [41]. Therefore, it is important to obtain nanocrystalline α -alumina also in other morphologies.

2.2 Sol-Gel Method

Sol-gel method is considered as a modern technique to prepare inorganic material via a chemical route [42]. The first sol-gel synthesis of silica was reported in 1846 by Ebelmen, a French chemist [43]. Till now, thousands of papers have been published and sol-gel chemistry has also opened new opportunities in the field of materials science [44].

2.2.1 Sol-Gel Method in Short

Sol-gel method normally involves the use of metal alkoxides or inorganic salts as precursors. Hydrolysis, condensation and polycondensation reactions occur when the precursors are mixed with water and solvents, as shown in figure 6, where M could be Al, Si, Ti, etc. A metal alkoxide precursor molecule is hydrolyzed first in the presence of water and solvent, for example ethanol. Hydrolysis results in the formation of (M-OH) group. These groups will further react to form (M-O-M) polymer in the condensation and polycondensation reactions, which leads to the formation of a sol suspension. In order to obtain homogeneous sol, it is important to optimize the hydrolysis rate by selecting a proper length and degree of the branching of the alkyl chain, and also controlling the mixing sequence and pH value of the suspension during the sol preparation [45].

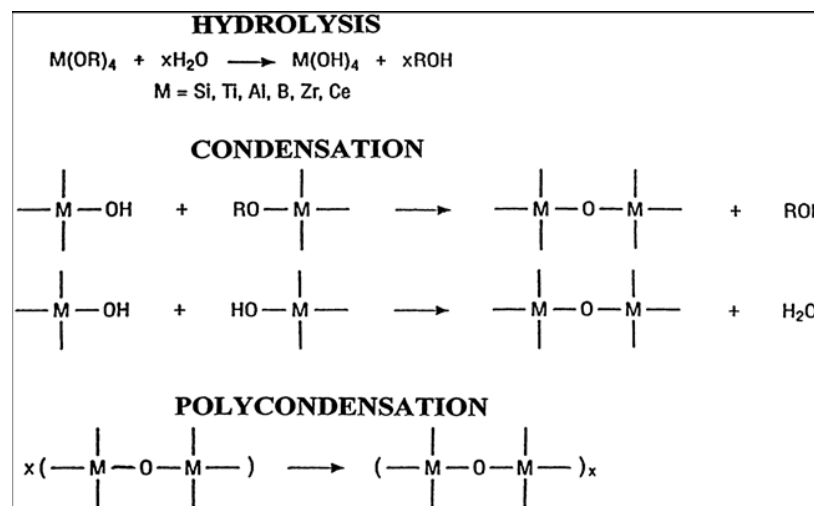


Figure 6 Reactions involved in the sol preparation [46].

Sol-gel method corresponds to a molecular way for materials science, which allows the design of the material (particle size, morphology, surface area, pore diameter, etc.) by controlling the conditions of the process (temperature, precursor, concentration of reagents, amount of water, drying methodologies, etc.) [3]. Sol-gel method has the advantages of high chemical purity, high chemical homogeneity, lower calcining temperatures and good control of particle size [47]. On the other hand, sol-gel method is a versatile method to synthesize not only powders but also thin films on various substrates. In case of alumina, figure 7 represents the steps leading to alumina powder and alumina film. The sol suspension can be dried to gel power, which can be calcined to form alumina powder, while from the same sol suspension, thin film can be prepared by dip/spin coating, which can be then calcined to form alumina film. Depending on the calcining temperatures, different alumina phases can be obtained.

The scheme illustration of the dip and spin coating process is shown in figure 8. Dip coating is a common and easy way to deposit a film on a substrate. The substrates could be

flat panels, cylinders or of complex geometry. The process could be utilized to coat areas in the order of square meters, and could be also operated in either continuous or batch modes [45]. While spin coating is an inherent batch process to produce thin films on a rigid flat or slightly curved substrate. The substrate used for this process is limited to a smaller size that can be held steadily for spinning at very high rotational speeds, i.e. 1000-4000 rpm [45].

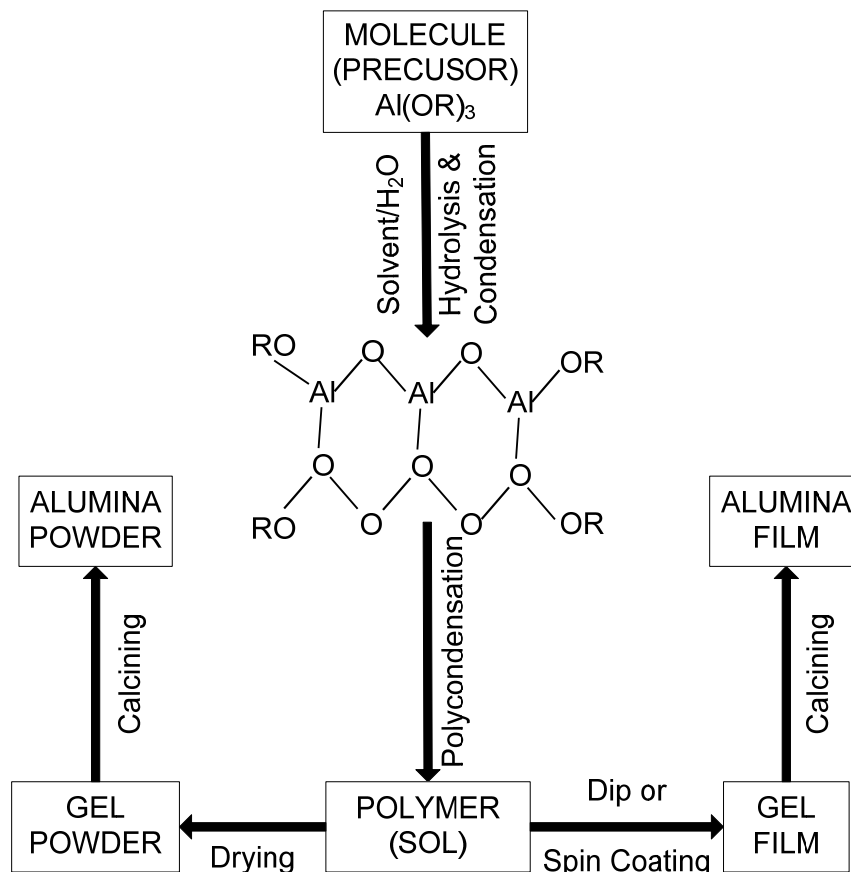


Figure 7 Flow chart of the illustration of the formation of alumina powder and film from the same sol suspension by sol-gel method.

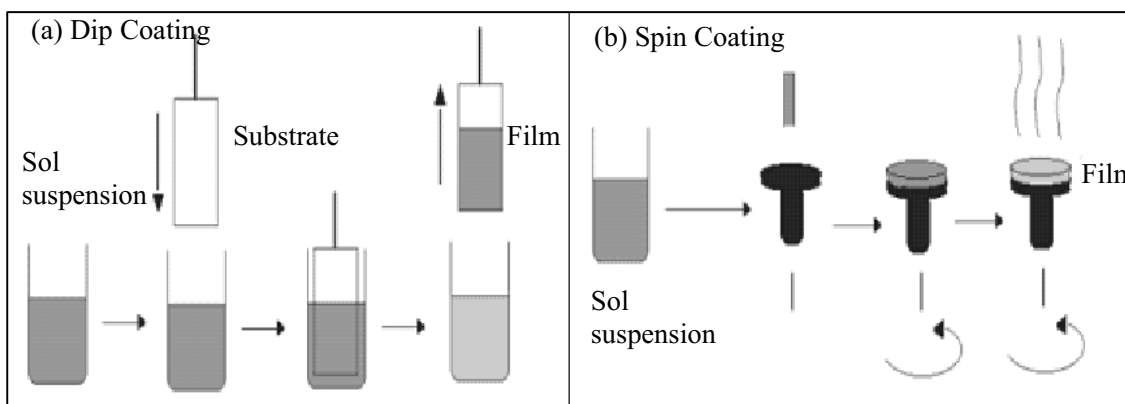


Figure 8 Illustration of the dip coating process in (a) and the spin coating process in (b) [48].

The main current industrial applications of the sol-gel method are the formation of thin films via dip or spin coating. The method of depositing films on flat glasses was patented in 1939, and the first product appeared on the market in 1953. Rear-view mirrors were commercialized in 1959, antireflective coatings in 1964 and sun-shielding windows in 1964. Many other sol-gel films have been commercialized for antistatic or optical applications and there is no doubt that sol-gel technology will find more applications in the future [44].

2.2.2 Sol-Gel Processing of Nanocrystalline α -Alumina Powder

Different aluminium alkoxides and solvents with possible additives as seeds have been used in different mixing sequences to prepare gel powder, which can be calcined at different temperatures to produce alumina in different polymorphs. The starting aluminium alkoxides, seed additives, sequence of mixing have influence on the particle size, morphology and formation temperature of the resulting α -alumina by calcining the gel powder. For example, Kim *et al.* [34] studied the effect of precursors and additives such as fluorides on the morphology of α -alumina.

Li *et al.* [38] obtained α -alumina powder at 1000 °C by using aluminium nitrate, water and citric acid with a molar ratio (citric acid to aluminium nitrate) of 2. The α -alumina had particle size of about 200 nm with plate-like morphology. Sharma *et al.* [40] synthesized α -alumina powder from 930 to 1170 °C depending on the pH value of the sol suspension by applying the precursors of aluminium isopropoxide, water and methoxyethanol with a seed additive of α -alumina. When pH was 2.5, the obtained α -alumina had particle size of 55-70 nm with spherical morphology and when pH was 12, the obtained α -alumina had particle size of 450-750 nm with hexagonal morphology. Gocmez and Özcan [37] reported the formation of α -alumina in size of about 50 nm by using aluminium nitrate, water and tartaric, oxalic, acetic acids from 925 to 1000 °C without seed. Liu *et al.* [35] succeeded to prepare particulate α -alumina in diameter of about 100 nm at 1150 °C by using aluminium isopropoxide, n-octyl alcohol, acetonitrile and water. Wu *et al.* [41] prepared plate-like α -alumina in size of 100 nm at 900 °C by using aluminium nitrate, polyethylene glycol and ammonia monohydrate with a seed additive of ZnF₂.

2.2.3 Nanocrystalline Boehmite Film by Boiling Water Treating the Gel Film

Tadanaga *et al.* [49-50] reported a sol-gel processing route to prepare the sol suspension by using aluminium tri-sec-butoxide, isopropyl alcohol, ethyl acetoacetate and water. Other than the conventional sol-gel route, after the spin coating, they heated the gel film and then treated the film with boiling water. After the boiling water treatment, flaky boehmite film was obtained. Tadanaga *et al.* [49-51] also studied the superhydrophobic and antireflective properties of such flaky film.

2.3 Superhydrophobic and Antireflective Applications

The structural and functional tailoring of materials from nanoscale to practical components has become an increasingly important topic due to the intensive research and development both in characterization and in advanced processing of materials. As part of this doctoral dissertation, superhydrophobic and antireflective applications have been studied.

2.3.1 Superhydrophobic Self-Cleaning Surface

Each year, huge amount of detergents are used for cleaning purpose in the whole world which is a burden to the environment. Self-cleaning or easy to clean surface is a good solution since it needs less chemicals or in best nothing but water and water is endless, safe, non-polluting, recyclable and environmentally friendly. The idea of superhydrophobic self-cleaning surface comes from nature, from lotus leaf. Every time after rain or in the morning with dew, the pearl-like water droplets remain on the lotus leaves. With breeze, the water droplets roll off from the leaves and take dirt away, as shown in figure 9. On such surface water droplet has a contact angle of more than 150° , and the surface is water-repellent and superhydrophobic. This phenomenon of self-cleaning, known as Lotus Effect, has long been known to many Asian cultures. For centuries, they have considered the lotus leaf as a symbol of purity due to its self-cleaning nature.

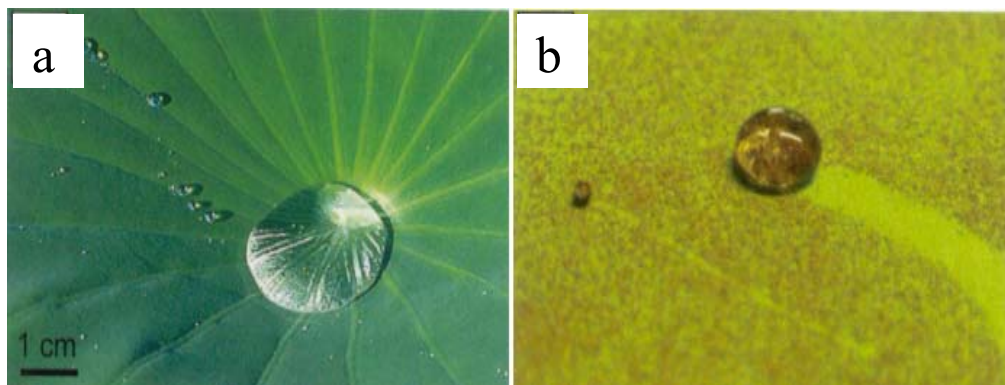


Figure 9 Water droplets on a lotus leaf in (a) and water droplets collect dirt from the surface of the lotus leaf in (b) [52].

To understand how the lotus leaf performs self-cleaning, scanning electron microscopy (SEM) was used to observe the microstructures on the lotus leaf. A SEM image of a lotus leaf is shown in figure 10 (a), where exists surface topography (i.e. roughness) both in microscale and in nanoscale, mainly composed of epicuticular wax crystals (with low surface energy) in combination with papillose epidermal cells [53]. A simple illustration of how self-cleaning works on a rough surface is given in figure 10 (b). The self-cleaning is functioned by the reduced contact area, thus the reduced adhesion between the dirt particles and the surface due to the surface roughness. However, the contact area, thus the adhesion between the dirt particles and the water droplet is larger. As a result, the dirt particles

adhere to the water droplet and are easily taken away when the water droplet rolls off from the surface. Therefore, the particulate depositions can be purified from the lotus leaf through rain, fog and dew [53].

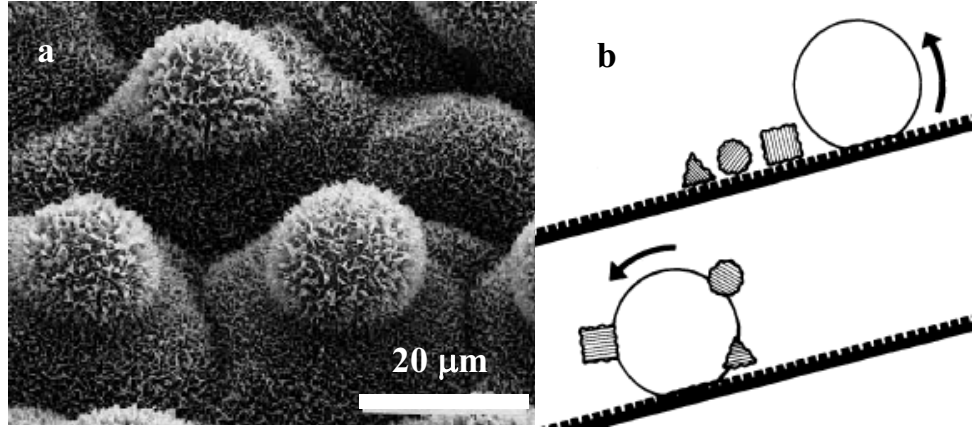


Figure 10 Scanning electron microscopy (SEM) surface image of a lotus leaf in (a) and illustration of how self-cleaning works on a rough surface in (b) [53].

The physics behind the Lotus Effect can be derived from the behavior of a liquid applied to a solid surface. The wetting of the solid is dependent on the relation shown in Young's equation:

$$\gamma_{SV} = \gamma_{SL} + \gamma_{LV} \cos \theta \quad (1)$$

where γ is the surface tension that is the energy per unit surface area of the interface. S, L and V represent solid, liquid and vapor, respectively. Therefore, γ_{SV} is the surface tension between the solid phase and the vapor phase, γ_{SL} between the solid phase and the liquid phase, and γ_{LV} between the liquid phase and the vapor phase. The angle θ is named as contact angle (CA) of the liquid on the given surface. When the liquid is water and the vapor is air, a CA of 0° means complete wetting and a CA of 180° corresponds to complete non-wetting. $0 < \theta < 90^\circ$ indicates the surface to be hydrophilic and $90^\circ < \theta < 180^\circ$ the surface to be hydrophobic. When $\theta < 5^\circ$, the surface is usually called to be superhydrophilic and when $\theta > 150^\circ$ the surface to be superhydrophobic [54].

Based on the Young's equation, when the surface energy of the solid is lowered, the CA is increased. However, surface energy is an intrinsic property of each material, and the common material with possibly the lowest surface energy (6.7 mJ/m^2 for a surface with regularly aligned closed-hexagonal-packed $-\text{CF}_3$ groups) gives a contact angle for water of only around 120° on a flat surface [55]. To obtain higher hydrophobicity, a proper surface roughness is required, as indicated by the lotus leaf. Two common models are normally used to describe the wetting on a rough surface. In the Wenzel model [56], the liquid is assumed to completely wet the grooves of a rough surface. The apparent contact angle θ_A (contact angle on a rough surface) is then given by

$$\cos \theta_A = r \cos \theta_Y \quad (2)$$

where r is the ratio of the actual area of the rough surface to the geometric projected 2-dimensional area, and θ_Y is the Young's contact angle on a flat surface. The equation thus states that a rough hydrophilic surface should be more hydrophilic, and a rough hydrophobic surface more hydrophobic than a flat surface with the same chemical composition. If air is trapped in the voids of a rough hydrophobic surface, the wetting can be described by the following equation simplified from the Cassie-Baxter equation [57]

$$\cos \theta_A = f_1 \cos \theta - f_2 \quad (3)$$

where f_1 is the surface area fraction of the solid material in contact with the liquid, θ the contact angle of the liquid on the pure solid material, and f_2 the surface area fraction of air in contact with the liquid ($f_1 + f_2 = 1$).

By learning from the lotus leaf and knowing the physics behind the Lotus Effect, low surface energy and proper surface roughness are two dominant factors to obtain superhydrophobic self-cleaning property. Therefore to obtain superhydrophobic self-cleaning surface, surface energy and surface roughness are two critical factors. By combining low surface energy and proper surface roughness, superhydrophobic self-cleaning surface could be obtained. There are mainly two possible ways to produce artificial superhydrophobic self-cleaning surface: one is to roughen a hydrophobic surface, and the other is to coat low surface energy molecules such as fluoroalkylsilanes on a rough surface [58-59]. However, only the surface with proper surface roughness (i.e. micro/nano structures) will present the superhydrophobic property.

2.3.2 Superhydrophobic Antireflective Surface

Since the early report of antireflective (AR) film in 1960s with a $\text{TiO}_2/\text{SiO}_2\text{-TiO}_2\text{-SiO}_2$ three-layer structure on a silicate glass substrate [60], AR films have raised great interest and many efforts have been reported on the preparation methods and their applications. Up to now, AR films have been applied on the cover glass of solar cells [60-62], glazings [63], windshields of automobiles [64], optical instruments [65] and so on. Especially in solar cell collectors reflection loss is a notable disadvantage that limits the energy efficiency. It is therefore necessary to reduce the reflection loss, that is, to increase the optical transmittance to improve the overall performance quality and efficiency.

According to the AR theory [66], using a single coating with a right thickness and refractive index, the reflectance at a specific wavelength can be reduced to a value near zero by satisfying the following relations:

$$n_f = \sqrt{n_s n_0} \quad (4)$$

$$t_f = \frac{\lambda_0}{4n_f} \quad (5)$$

where n_f , n_0 , n_s are the refractive indices of the film, the environmental medium and the substrate, respectively, and t_f is the film thickness and λ_0 the wavelength at which the reflection is near zero.

Typical soda-lime glass has a refractive index of 1.5. Based on the equation (4), an antireflective film on glass in air must have a refractive index of 1.23 which gives a zero reflection at a specific wavelength with a specific film thickness. Unfortunately the lowest refractive index of the readily available material is limited to about 1.35 [67]. Furthermore, the applications of such AR films are limited especially in solar cells since they are only antireflective at one wavelength. In solar cells it is critical to have broadband antireflection to increase the energy efficiency. Although a multi-layer film can be deposited to increase the bandwidth over which the low reflection loss can be obtained, it normally adds some complexity to the producing process. Therefore simple synthesis of broadband AR film is warmly welcomed. To solve this problem, the manufacturing of porous film is a good solution. This idea comes from natural moth eye and butterfly eye structure, as shown in figure 11. The corneal surface of the moth and butterfly eye has nano-scaled hexagonal protuberances. As a result, the moth and butterfly eye has very low reflectance and can absorb light from any directions.

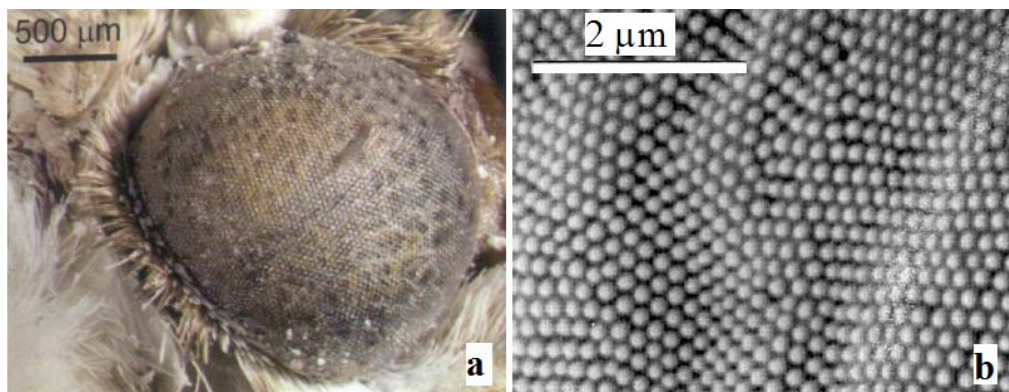


Figure 11 Scanning electron microscopy (SEM) image of a moth eye in (a) [52], and the antireflective corneal surface of a butterfly eye in (b) [68].

The refractive index of a material is related to its density, therefore when lowering the density by introducing pores the refractive index is also lowered. Moreover, it is required that the pore size should be much smaller than the wavelength of the light, and the pores should be homogeneously distributed in order not to affect the light transmission and cause scattering [69]. At the same time, to achieve the broadband AR film, there should be graded porosity which results in a gradual change in density and further in refractive index through the film, thus minimizing the reflection loss [67].

For the normal porous silica AR films, the adsorption of water vapor into the hydrophilic pores increases the refractive index and then lowers the antireflection, which limits the

lifetime of the porous silica AR films. The solution is to combine the superhydrophobic property with the antireflective property. Then the films are repellent to water and have a good performance. Therefore it is beneficial and necessary to realize antireflective and superhydrophobic properties simultaneously to the same film.

2.3.3 Processing of Superhydrophobic Surface

As mentioned beforehand, the processing of superhydrophobic surface could be divided into two categories. In the first category, hydrophobic materials with certain surface topography/roughness are used. For example, Xie *et al.* [70] reported a simple one-step casting process to produce a superhydrophobic surface from poly (methyl methacrylate) and fluorine-end-caped polyurethane in air under ambient atmosphere by utilizing the solubility difference of the two polymers in a solvent of demethylformamide. Zhang *et al.* [71] obtained a superhydrophobic film by extending a Teflon film to about 190% with the increase of water contact angle from 118 to 165°. Erbil *et al.* [72] described the formation a superhydrophobic coating using polypropylene by selecting suitable solvents and temperature to control the surface roughness. The resulting gel-like porous coating had a water contact angle of 160°. Lu *et al.* [73] obtained a low-density polyethylene superhydrophobic surface by controlling the crystallization of the low-density polyethylene. Other than the different polymers used in the first category, inorganic materials are commonly used in the second category to obtain superhydrophobic surface by depositing a top layer of fluorosilane on the roughened surface to modify the surface chemistry. It opens the possibility to apply different inorganic materials such as boehmite, alumina, titania, silica, carbon nanotubes by using different processing methods for example lithography, sol-gel process, chemical vapor deposition, and so on [49-50, 74-79].

2.3.4 Challenges of the Artificial Superhydrophobic Surface

The main challenge of the artificial superhydrophobic surface is its durability. The superhydrophobicity is introduced by the surface micro/nano structures which are not as durable as bulk materials in practical applications. The plants and animals can do self-repair for the destroyed surface. However, the artificial surface cannot do self-repair easily by itself. The practical surface must withstand touching or rubbing, as well as environmental contamination. Meanwhile, the manufacturing process has to be quick and simple. Therefore, a lot of efforts are still required from researchers and scientists to accomplish the goal.

3. MATERIALS AND METHODS

Based on the idea of boiling water treatment of the spin-coated film from Tadanaga *et al.* [49-50], flaky boehmite powder was obtained in this dissertation by treating the gel powder with boiling water. By calcining the flaky boehmite powder at different temperatures for different hours, nanocrystalline γ -, δ -, θ - and α -alumina powders with different morphologies were obtained, studied and discussed. Nanocrystalline α -alumina was also prepared by calcining the gel powder.

Moreover, flaky boehmite film was reproduced on austenitic stainless steel and glass based on Tadanaga *et al.*'s process. Besides, more work was done to study the formation process, and more characterization was carried out to understand in more detail about the superhydrophobic and antireflective properties.

The main processing steps in the dissertation are illustrated in figure 12, which is modified from the conventional sol-gel processing route in figure 7. An overview of the experimental procedures and the characterization methods used in the doctoral dissertation is shown in figure 2.

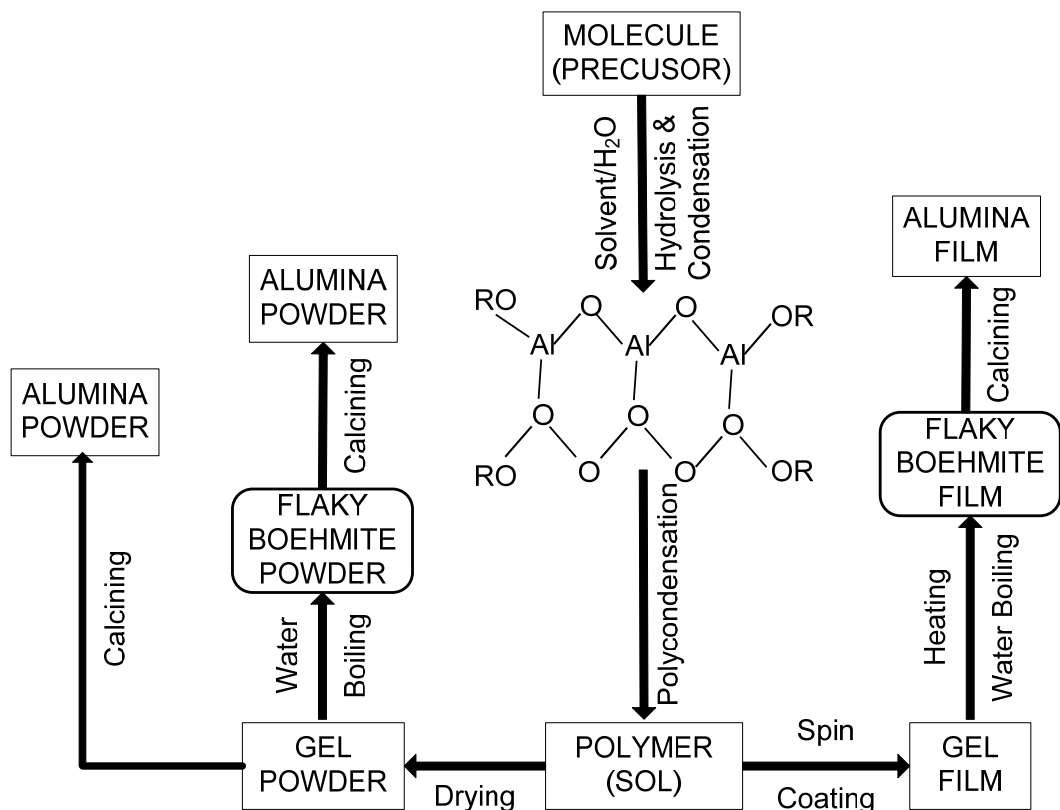
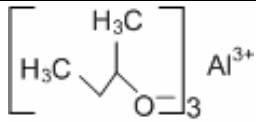
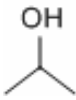
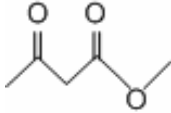
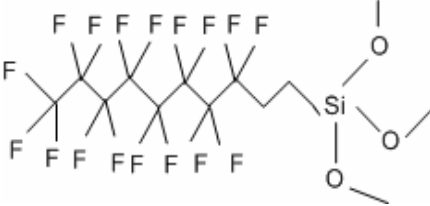


Figure 12 Illustration of the main processing steps in the dissertation.

3.1 Materials

The starting materials to prepare the sol suspension were aluminium tri-sec-butoxide (denoted as $\text{Al}(\text{O-sec-Bu})_3$, $\text{C}_{12}\text{H}_{27}\text{AlO}_3 > 97\%$, VWR), isopropyl alcohol (denoted as i-PrOH, $\text{C}_3\text{H}_7\text{OH} > 99\%$, VWR) and ethyl acetoacetate (denoted as EAcAc, $\text{C}_6\text{H}_{10}\text{O}_3 > 98\%$, VWR). The surface chemistry of the film was modified by (heptadecafluoro-1,1,2,2-tetrahydrodecyl)trimethoxysilane ($\text{CF}_3(\text{CF}_2)_7\text{CH}_2\text{CH}_2\text{Si}(\text{OCH}_3)_3$, denoted as FAS, ABCR GmbH & Co. KG, Karlsruhe, Germany). The structural formulas and other information of these above-mentioned starting materials are given in table 2.

Table 2 The chemical formulas, structural formulas, molecular weights and CAS numbers of the starting materials in the experiments.

Chemical Name	Chemical Formula	Structural Formula	Molecular Weight	CAS Number
Aluminium tri-sec-butoxide	$\text{C}_{12}\text{H}_{27}\text{AlO}_3$		246.32	2269-22-9
Isopropyl alcohol	$\text{C}_3\text{H}_7\text{OH}$		60.10	67-63-0
Ethyl acetoacetate	$\text{C}_6\text{H}_{10}\text{O}_3$		130.14	141-97-9
(Heptadecafluoro-1,1,2,2-tetrahydrodecyl)trimethoxysilane	$\text{CF}_3(\text{CF}_2)_7\text{CH}_2\text{CH}_2\text{Si}(\text{OCH}_3)_3$		568.30	83048-65-1

3.2 Experimental

Flow charts of the experimental procedures are shown in figures 2 and 12. The following are some brief explanations concerning to some of the steps.

3.2.1 Sol Suspensions

Two different sol suspensions (sol A and sol B) were prepared. In sol A, 3 g $\text{Al}(\text{O-sec-Bu})_3$ and 50 ml i-PrOH were mixed and in sol B 3 g $\text{Al}(\text{O-sec-Bu})_3$ and 30 ml i-PrOH were used. After mixing them for 1 h, 2 ml EAcAc was introduced, and then the solution was stirred

for 1 h. After that, the mixture of 1 ml water and 5 ml i-PrOH was added for hydrolysis and with mixing for another 2 h the sol suspension was ready for the following procedures.

3.2.2 Gel Powder and Flaky Boehmite Powder

The sol suspension sol B was dried at 120 °C into fine powder, which is named as gel powder. The gel powder was then reacted with boiling water for 10 min to form boehmite. The boehmite-containing suspension was then dried at 120 °C to obtain fine flaky boehmite powder.

3.2.3 Calcinations of the Gel Powder and the Flaky Boehmite Powder

The gel powder was calcined in a tube furnace at 1000 °C from 0.5 h to 6 h in air with a heating rate of 13 °C/min and a cooling in furnace. While the flaky boehmite powder was calcined from 500 to 900 °C for 6 h, and at 1000 °C from 1 h to 40 h under the same condition as for the gel powder.

3.2.4 Spin Coating

Spin coating was carried out from the sol suspension sol A and sol B at 1500 rpm for 20 s to deposit a gel layer. When needed, a second gel layer was spin-coated on the top of the first gel layer after the first gel layer was heat-treated at 400 °C for 30 min.

3.2.5 Substrates

One type of substrate was AISI 316-2B austenitic stainless steel, which was firstly cleaned in acetone and then in ethanol ultrasonically for 10 min, and finally rinsed with deionized water. The surface of the austenitic stainless steel is not smooth in microscale and grain boundaries can be clearly seen under SEM due to the pickling of the stainless steel in the production process. The other type of substrate was Wenzel Glaser microscope glass slide, which was cleaned in the same way as the austenitic stainless steel substrate.

3.2.5 Formation of Nanocrystalline Flaky Boehmite Film

The gel film was pre heat-treated at different temperatures from room temperature (RT) to 900 °C for 15 min, which was then immersed into boiling water for 10 min to react with water to form flaky boehmite film. The as-prepared film was then either post heat-treated at different temperatures from 100 to 900 °C for 30 min and then FAS treated or directly treated with hydrolyzed FAS.

3.2.6 Modification of Surface Chemistry

The surface chemistry of the as-synthesized films was finally modified by FAS. The FAS solution was prepared by mixing 1 ml FAS and 50 ml ethanol for 1 h. Then the film was immersed into the FAS solution for 1 h, followed by heating at 180 °C for 1 h in air.

3.3 Characterization Methods

Various characterization methods were used in this dissertation. The different testing methods of each sample can be checked from the flow chart in figure 2. The following are some brief descriptions of the characterization methods.

3.3.1 X-Ray Diffraction (XRD)

The crystalline phases were determined by X-ray diffraction (XRD, Kristalloflex D-500, Siemens) by using Cu K α radiation with a step size of 0.01° and a count time of 1 s per step. Slow scans with a step size of 0.005° and a count time of 10 s per step were also used to further check the crystalline phase of the sample. The crystallite size d_{XRD} was evaluated from the XRD pattern by using Scherrer equation, $d_{\text{XRD}} = K\lambda / (\text{FWHM})\cos\theta$, where $K=0.9$, $\lambda=1.5406 \text{ \AA}$, FWHM is the full width at the half maximum of the diffraction peak and θ is the diffraction angle, also called Bragg angle. Normally, the strongest diffraction peak of the sample was used to estimate d_{XRD} .

3.3.2 Field Emission Scanning Electron Microscopy (FESEM)

Morphology was examined by field emission scanning electron microscopy (FESEM, Hitachi S-4800). A thin film (1-2 nm) of Pt/Pd alloy (80/20) was sputtered on the sample to avoid charging. The cross-sectional FESEM images were used to measure the film thickness and reveal the surface topography.

3.3.3 Transmission Electron Microscopy (TEM) and Selective Area Electron Diffraction (SAED)

The morphology was also examined by transmission electron microscopy (TEM, Jeol JEM 2010) in which selected area electron diffraction (SAED) was used to analyze the phase structure. The TEM samples in the film processing were prepared in the following way. The stainless steel was pre-thinned mechanically by different SiC grinding papers with grit sizes from 120 to 1200 to a thickness of 0.1 mm. Then disks with diameters of 3 mm were cut from the pre-thinned steel plate by a disc punch (model 310, South Bay Technology Inc.). A small hole was made in the center of the disk by final thinning, which was done by a Tenupol 5 twin jet electrolytic polisher (Struers) using a solution of nitric acid in methanol (1:2) at -50 °C. The film was made on the disk by the same procedures as on the stainless steel substrate. In this way, the film on the edge area of the central hole was thin enough to be observed in TEM.

3.3.4 High Resolution Transmission Electron Microscopy (HRTEM)

Morphology and phase structure were also studied by high resolution transmission electron microscopy (HRTEM, Tecnai F20 S-Twin). The fast Fourier transform (FFT) analysis of the lattice images was carried out by image analysis software, Gatan DigitalMicrograph Suite.

3.3.5 Gas Adsorption/Desorption Test

Nitrogen adsorption/desorption isotherms were obtained by using a gas sorption experiment (Coulter Omnisorp 100 CX, Beckman Coulter Inc.) at the temperature of liquid nitrogen. The samples were degassed at 200 °C prior to the measurement. The data analysis was carried out with a Coulter SA-reportsTM software. The specific surface areas were calculated by the Brunauer-Emmett-Teller (BET) equation [80] using the data in the P/P₀ range of 0.05-0.4. The pore size distribution curves in meso range (3-100 nm) were obtained by a Barrett-Joyner-Halenda (BJH) model [80] from the desorption branches of the isotherms. The particle size d_{BET} was evaluated by using equation $d_{\text{BET}}=6/(\rho S)$ where ρ is the density of the solid and S is the BET surface area, assuming the particles to be spherical or cubic.

3.3.6 Thermogravimetry-Differential Scanning Calorimetry (TG-DSC)

Thermal analysis of the gel powder was studied by thermogravimetry-differential scanning calorimetry (TG-DSC, STA 409, Netzsch) from 30 to 1200 °C with a heating rate of 10 °C /min. The sample weight was 20.1 mg.

3.3.7 Atomic Force Microscopy (AFM)

Surface topography of the film was observed by atomic force microscopy (AFM, Nanoscope IIIa, Digital Instruments, Santa Barbara, CA). All the images were recorded in a tapping mode using silicon cantilevers with a resonance frequency between 250 and 300 kHz. All the images (512*512 pixels) were measured in air without filtering. The scanning probe image processor software (SPIP, Image Metrology, Denmark) was used for the analysis of the image. A set of roughness parameters has been developed and standardized for versatile characterization of various surface properties [81]. The root-mean-square roughness S_q is the most widely used amplitude roughness parameter that gives the standard deviation of height. Surface skewness S_{sk} describes the asymmetry of the height distribution. A zero value of S_{sk} represents a Gaussian-like surface. Negative value of S_{sk} refers to a porous surface, that is, the valleys dominate over the peak regimes. Respectively, the local summits dominate over the valleys when $S_{sk} > 0$. Two hybrid parameters have been developed to especially describe the forms of the summits: the mean summit curvature, S_{sc} , and the root-mean-square value of the surface slope, S_{dq} . Most of the above-mentioned parameters contribute to the effective surface area: the absolute height difference, the number and form of the local maxima, among others. A measure for the effective surface area with respect to the projected area is given in percent by the surface area ratio parameter S_{dr} .

3.3.8 Contact Angle Measurement

Water contact angles were measured by a system (Pisara, FotoComp Oy, Jyväskylä, Finland), which is composed of a microliter syringe for releasing the water droplet and an optical system connected to a computer for data analysis. The size of the water droplet was

5 μl in the measurement. Droplets were placed at five positions and the average value was accepted as the final contact angle value.

3.3.9 Ultraviolet-Visible Spectrophotometry (UV-Vis Spectrophotometry)

Optical transmittance spectra of the films were measured with a UV-visible spectrophotometer (Shimadzu UV-2501PC, Japan) over the wavelength range of 190-900 nm.

3.3.10 Optical Profilometry

Thickness of the FAS layer on glass was examined by an optical profilometer (Wyko NT1100, Veeco, USA).

4. RESULTS AND DISCUSSION

In this chapter, the main results in the attached 7 original publications are summarized. At first, nanocrystalline transition alumina (γ -, δ -, θ -alumina) powders with high surface areas in morphologies of nanorods and nanoparticles were synthesized and characterized. Then nanocrystalline α -alumina powder with novel morphology was obtained at a relatively low temperature of 1000 °C without using seed additive, while the formation scheme of the morphology and the phase transformation from θ - to α -alumina was discussed. Besides, nanocrystalline α -alumina in nearly spherical morphology was also synthesized. Finally boehmite and alumina films were processed and studied for the superhydrophobic and antireflective applications.

4.1 Nanocrystalline Transition Alumina Nanoparticles and Nanorods

Flaky boehmite (γ -AlOOH) powder was obtained by treating the gel powder with boiling water. The flakes have thicknesses of about 5 nm and lengths and widths of about 100 nm, as shown in figure 13.

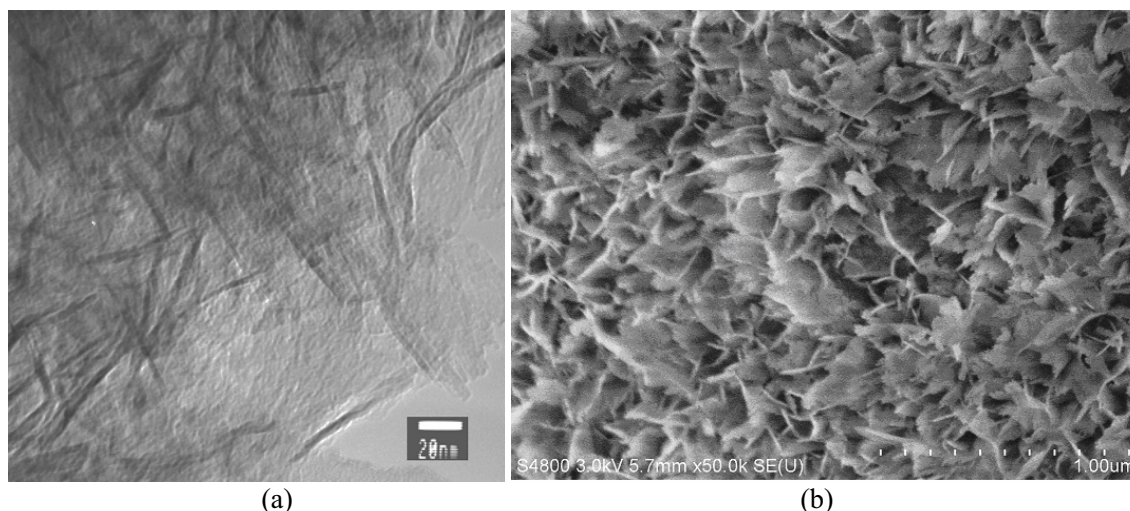


Figure 13 Transmission electron microscopy (TEM) image in (a) and field emission scanning electron microscopy (FESEM) image in (b) of the flaky boehmite powder [I].

By calcining such flaky boehmite powder from 500 to 900 °C for 6 h and at 1000 °C for 1 h, different transition alumina (γ -, δ -, θ -alumina) powders were obtained, see the XRD patterns in figure 14. The gel powder is amorphous, since it is difficult to index the three very broad peaks in the pattern. After reaction with boiling water, boehmite (γ -AlOOH) was formed which was confirmed according to the JCPDS data (File card No. 74-1895). When the flaky boehmite powder was heat-treated at 500 °C for 6 h, boehmite disappeared. When the heat-treatment temperatures were further increased, the diffraction peaks get a

little sharper and more peaks show up for the samples calcined at 900 and 1000 °C. However no peaks are due to α -alumina. All the diffraction peaks exhibit high degree of broadness due to the formation of nanocrystallites. The temperature dependent peak sharpening can be related to the growth of the crystallites. The crystallite size can be estimated by using the Scherrer equation. The calculation was based on the diffraction peak 200 centered on the 2θ value of 48° for boehmite, and the diffraction peaks centered on the 2θ value of 67° for others. Boehmite has the crystallite size d_{XRD} of 3.9 nm, and after calcination, the crystallite size d_{XRD} is 3.9 nm at 500 °C, 4.0 nm at 600 °C, 4.2 nm at 700 °C, 4.7 nm at 800 °C, 5.2 nm at 900 °C and 5.9 nm at 1000 °C.

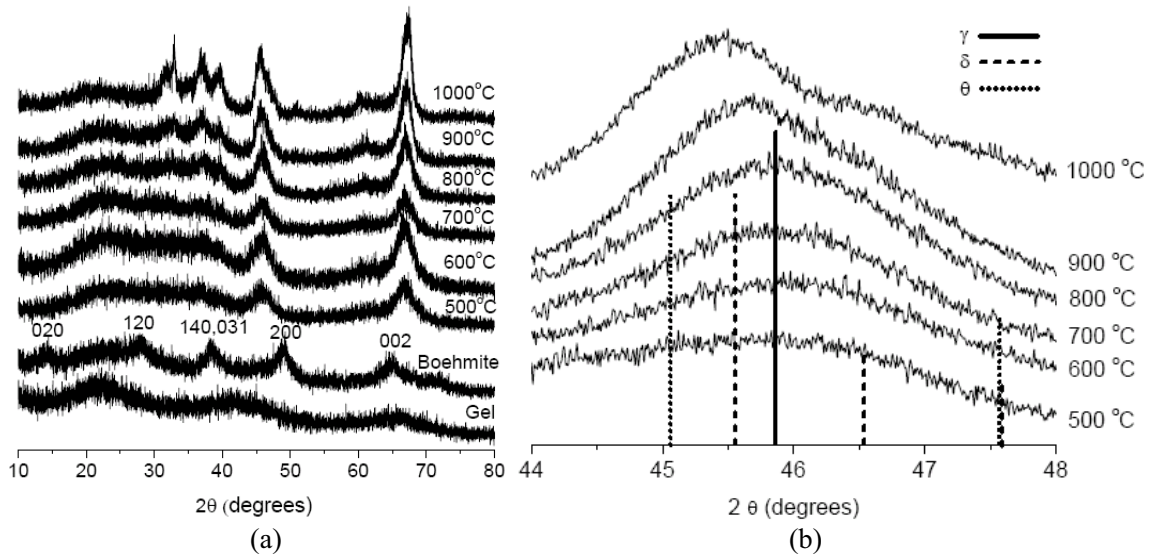


Figure 14 X-ray diffraction (XRD) patterns of the gel powder, the flaky boehmite powder and of the flaky boehmite powder calcined from 500 to 900 °C for 6 h and at 1000 °C at 1 h in (a). Slowly scanned XRD patterns of the samples from 500 to 1000 °C are shown in (b) [1].

As known, when boehmite is the starting material for calcinations, the phase transformation sequence is γ -, δ -, θ - and finally α -alumina [10]. The solid vertical line in figure 14 (b) shows the place of the diffraction peak for γ -alumina (JCPDS card No. 10-425), dashed vertical line for δ -alumina (JCPDS card No. 4-877) and dotted vertical line for θ -alumina (JCPDS card No. 11-517). The strongest diffraction peak of γ -alumina is at the 2θ value of 45.8° , while the second strongest diffraction peaks of δ - and θ -alumina are at the 2θ values of 45.5° and 45.0° , respectively, according to their JCPDS data. This is indicated by the different lengths of the vertical lines from 45° to 46° . Based on the phase transformation sequence, as shown in figure 14 (b), γ -alumina was formed from 500 to 800 °C. When the flaky boehmite powder was calcined at 900 °C, δ -alumina was formed. The diffraction peak is not exactly at the same position as the dashed vertical line for δ -alumina, indicating that γ -alumina coexisted with δ -alumina. When the calcination temperature was 1000 °C, more γ -alumina transformed to δ -alumina and some δ -alumina transformed to θ -alumina. However, it is possible that small amount of γ -alumina still existed in the sample.

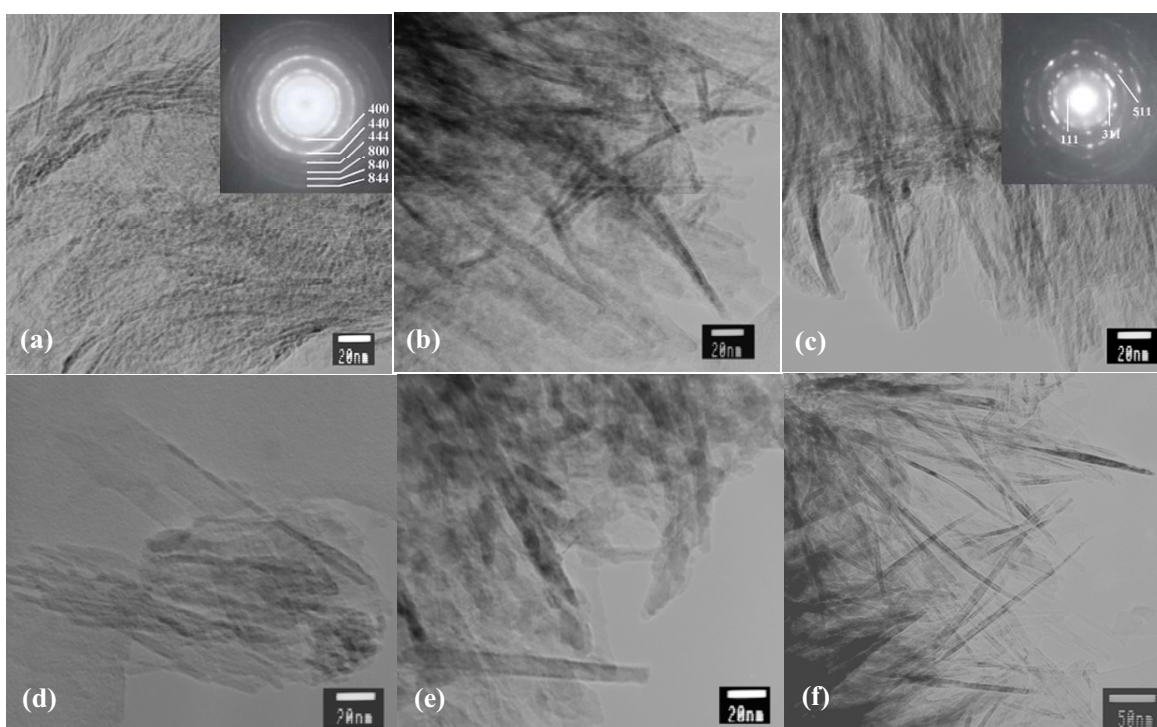


Figure 15 Transmission electron microscopy (TEM) images of the flaky boehmite powder calcined at 500 °C (a), 600 °C (b), 700 °C (c), 800 °C (d), 900 °C (e) and 1000 °C (f). The inserted SAED patterns in (a) and (c) are indexed according to γ -alumina. Bars = 20 nm in (a-e) and bar = 50 nm in (f) [1].

The morphologies of the different transition aluminas (γ -, δ -, θ -alumina) obtained at different temperatures are shown in figure 15. When the flaky boehmite powder was calcined at 500 °C, boehmite was converted into γ -alumina. The SAED pattern further confirms the formation of γ -alumina, as indexed in figure 15 (a). The rings in the SAED pattern result from the formation of nanocrystalline γ -alumina. When the flaky boehmite powder was calcined at 600 °C, the phase did not change, but the morphology changed to nanorods. The estimated crystallite size d_{XRD} of the γ -alumina at 600 °C is 4.0 nm, which indicates that the individual nanorod is composed of several crystallites.

High resolution transmission electron microscopy (HRTEM) was also applied to study the morphology of the nanocrystalline γ -alumina obtained by calcining the flaky boehmite powder at 600 °C for 6 h, as shown in figure 16, where the image in (a) was taken at a low magnification and the image in (b) at a high magnification. The γ -alumina has the morphology of nanorods with lengths of about 300 nm and widths of 10 nm. However, in the image (b), the crystallites of 4 nm in size are observed, and the crystallites also arrange themselves into a rod with width of 10 nm. The evaluated d_{XRD} of the γ -alumina is 4.0 nm, which agrees well with the crystallites seen in the image in figure 16 (b). The FFT pattern inserted in (c) was taken from the whole image area. The spots in the FFT pattern form a discontinuous ring, which corresponds to γ -alumina. The enlarged view of the squared area

in (c) is shown in (d) where the lattice images of two crystallites can be clearly observed. The calculated plane spacing is 2.28 Å for both crystallites, which corresponds to the (222) plane of γ -alumina.

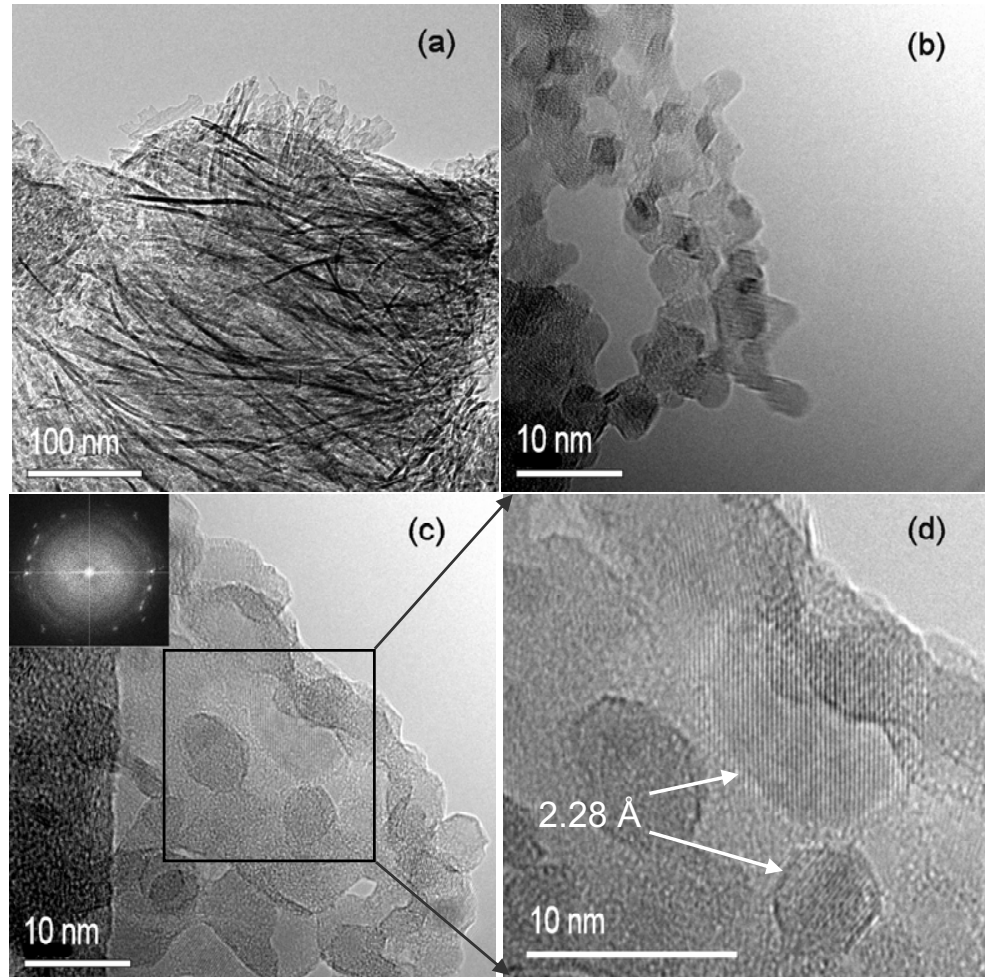


Figure 16 Images of the γ -alumina obtained by calcining the boehmite powder at 600 °C for 6 h. The FFT pattern is inserted in (c) and indexed to be γ -alumina. The enlarged view of the squared area in (c) is shown in (d), where the calculated plane spacing corresponds to the (222) plane of γ -alumina [III].

When calcined at 700 °C and 800 °C, the morphology remained to be nanorods. More rings and more spots occur in the SAED pattern in figure 15 (c), which is due to γ -alumina. When the flaky boehmite powder was calcined at 900 °C, δ -alumina coexisted with γ -alumina. The TEM image shows that the nanorods have widths of about 10 nm. When the flaky boehmite powder was calcined at 1000 °C, θ -alumina started to form, which coexisted with δ -alumina, possibly also γ -alumina. The nanorods are better shaped, with lengths of about 300 nm and widths of about 10 nm. The formation of nanorods may undergo the Ostwald ripening process in which larger crystallites grow at the expense of smaller crystallites being dissolved [82].

The morphology of the transition alumina obtained by calcining the flaky boehmite powder at 1000 °C for 1 h was also characterized by HRTEM, with the images shown in figure 17. Crystallites of about 5 nm in size can also be observed on the surface of the nanorods. The evaluated d_{XRD} is 5.9 nm which is in good agreement with the crystallites shown in the image. The morphology of the sample at 1000 °C for 1 h follows that of the γ -alumina obtained at 600 °C for 6 h, as shown in figure 16, only with slightly larger crystallites.

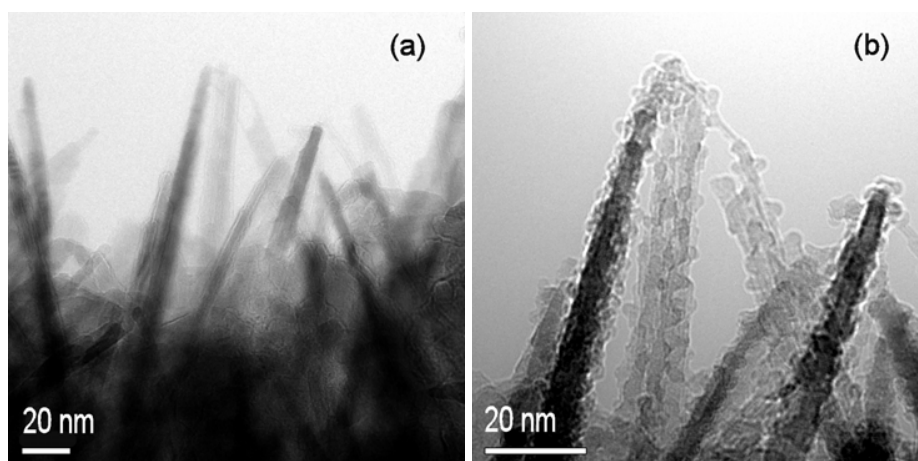


Figure 17 Images of the transition alumina prepared by calcining the flaky boehmite powder at 1000 °C for 1 h [III].

The N_2 adsorption/desorption isotherms and the pore size distribution curves of the samples are shown in figure 18. The isotherm of the gel powder with a BET surface area of 576 m^2/g is characterized as type I isotherm with a plateau which is nearly horizontal, and the adsorption mostly happens at very low P/P_0 . Type I isotherm is related to micropores [83]. When the gel powder reacted with boiling water, the flaky boehmite powder was obtained which gives a type IV isotherm with a H4 hysteresis loop and has a BET surface area of 303 m^2/g . Type IV isotherm can be correlated with mesopores [83]. However, the high adsorption at very low P/P_0 indicates also the existence of a considerable amount of micropores. When calcining the flaky boehmite powder from 500 to 1000 °C, all samples show type IV isotherms with H2 hysteresis loops which are believed to occur in the systems where the pores have narrow necks and wide bodies (i.e. “ink-bottle”) or when the porous material has an interconnected pore network [84]. The change in the shape of the hysteresis loop can be correlated with the change in the pore structure which is related to the phase change from boehmite to transition aluminas with different morphologies. The BET surface areas of the transition aluminas are 438 m^2/g at 500 °C, 320 m^2/g at 600 °C, 267 m^2/g at 700 °C, 200 m^2/g at 800 °C, 124 m^2/g at 900 °C and 79 m^2/g at 1000 °C. The surface areas of the γ -alumina at 500 to 700 °C are larger than those normally observed for conventional γ -alumina (189-255 m^2/g) [23]. When the flaky boehmite powder (BET surface area 303 m^2/g) was calcined at 500 °C, dehydroxylation started and hydrogen bonds disintegrated, resulting in the formation of γ -alumina with increased BET surface area.

When the calcination temperature was further increased, the Ostwald ripening might happen and the agglomerated crystallites were sintered denser, leading to the progressive reduction in BET surface area. When the flaky boehmite powder was calcined at 500 °C, the high adsorption at low P/P_0 indicates a large microporosity, however the well-defined step in the desorption branch of the isotherm indicates a pore size of 3.9 nm, as seen in the pore size distribution in figure 18 (b). When the flaky boehmite powder was heat-treated at 600-900 °C, the pore size increases slightly to 4.1 nm, see figure 18 (b). When the flaky boehmite powder was calcined at 1000 °C, the sample has a larger pore size of 6 nm with a broader pore size distribution. The pores could be attributed to intercrystallite spaces of the nanoparticles and nanorods as shown in figure 15.

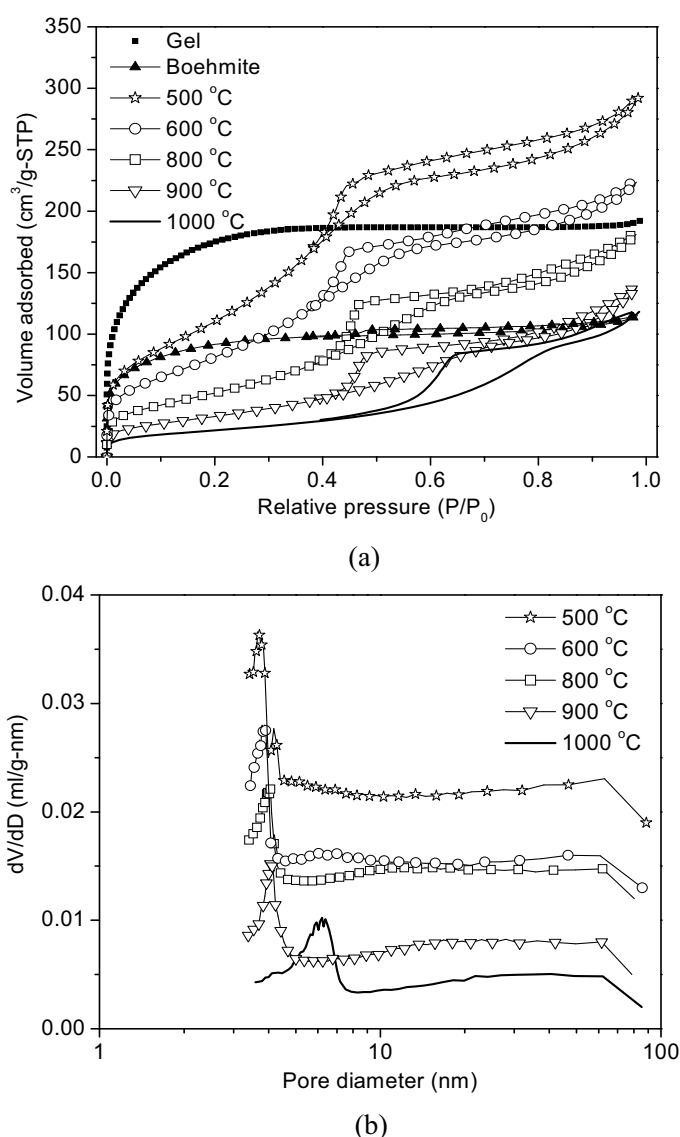


Figure 18 Typical N₂ adsorption/desorption isotherms of the gel powder, the flaky boehmite powder, and of the flaky boehmite powder calcined at 500, 600, 800, 900 and 1000 °C in (a) and the pore size distribution curves of the flaky boehmite powder calcined at 500, 600, 800, 900 and 1000 °C in (b) [I].

4.2 Nanocrystalline α -Alumina at 1000 °C from Flaky Boehmite Powder

By calcining the same flaky boehmite powder, nanocrystalline α -alumina powder can be obtained. The phase transformation to α -alumina cannot be completed at 900 °C even with a very long dwell time of 160 h. When the calcination temperature was 1000 °C, as shown in the XRD patterns in figure 19, no peaks of α -alumina were observed with a dwell time of 1 h, and the sample was a mixture of transition alumina (δ - and θ -alumina, perhaps also γ -alumina). For 5 h, α -alumina started to form with the coexistence of transition alumina. For 20 h and 30 h, more and more α -alumina was formed, and for 40 h, the phase transformation to α -alumina was finally completed. It is difficult to determine whether the transition alumina is γ -, or δ - or θ -alumina, due to the very few and very broad diffraction peaks from the transition alumina in the XRD patterns in figure 19. On the other hand, when the calcination temperature was further increased to 1100 °C, the phase transformation to α -alumina was completed with a dwell time of 1 h.

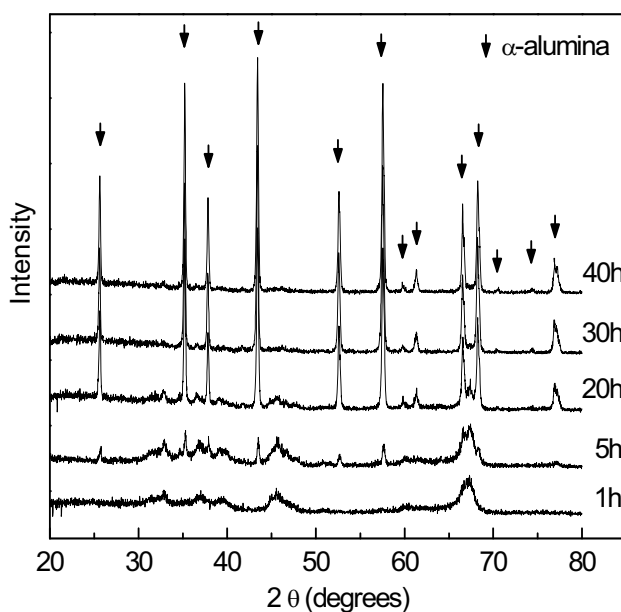


Figure 19 X-ray diffraction (XRD) patterns of the alumina powders obtained by calcining the flaky boehmite powder at 1000 °C for different hours. The arrows signify the diffraction peaks from α -alumina [III].

4.2.1 Morphology Analysis

The morphology of the transition alumina obtained at 1000 °C for 1 h is shown in figure 17, where crystallites of about 5 nm in size can be seen on the surface of the nanorods. When the flaky boehmite powder was calcined at 1000 °C for 20 h, more α -alumina was formed together with θ -alumina, with the morphology shown in figure 20. It is supposed here that all the δ -alumina transformed to θ -alumina for simplicity, though there might be a small

amount of δ -alumina left in the sample. The image in a low magnification is shown in figure 20 (a), where the nanorods grow wider to about 20 nm and some nanoparticles show up. In the image in figure 20 (b), crystallites of 5 nm in size can be seen. The image in figure 20 (c) shows a nanorod with width of about 20 nm, where the crystallites of 5 nm can be seen on the surface of the rod. The calculated plane spacings of 5.42 Å and 4.52 Å correspond to the planes (001) and (201) of θ -alumina, respectively.

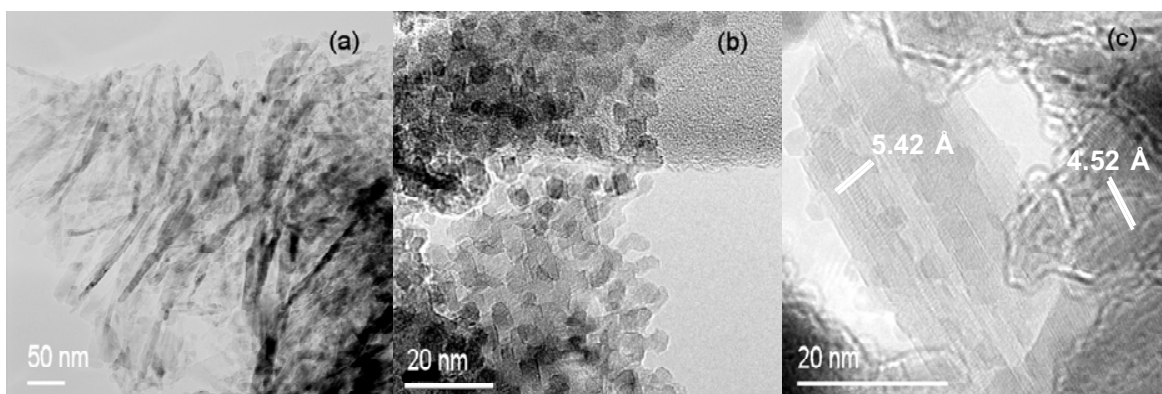


Figure 20 Transmission electron microscopy (TEM) images of the alumina prepared by calcining the flaky boehmite powder at 1000 °C for 20 h. The plane spacings of 5.42 Å and 4.52 Å correspond to the planes (001) and (201) of θ -alumina [III].

When the flaky boehmite powder was calcined at 1000 °C for 40 h, pure α -alumina phase was formed. The morphology of the α -alumina powder is given by the TEM and FESEM images in figure 21, where the nanorods coexist with the nanoparticles in (a) and separate views of the nanorods and the nanoparticles are shown in (b) and (c). Synthesis of spherical and plate-like α -alumina has been reported frequently [35-40], however, it is quite rare for α -alumina to form into nanorods. More interestingly and surprisingly, the nanorods are actually composed of many nearly spherical nanocrystallites as shown in figure 22. The nanocrystallites are in diameters of about 5 nm.

Lattice image of one 5 nm-crystallite is presented in figure 23 (a), where the corresponding FFT pattern is inserted. The lattice fringes in the HRTEM image reveal that the 5 nm-crystallite is of a single crystallite. The FFT pattern is indexed to be hcp crystal system with a beam direction of $[\bar{1}2\bar{1}1]$, which confirms that the 5 nm-crystallite is α -alumina. Two other crystallites with diameters of about 8 nm are shown in figure 23 (b) and the plane spacing of 2.38 Å is due to the plane $(11\bar{2}0)$ of α -alumina. This is the first report of α -alumina crystallite less than 10 nm and this may possibly induce new discussions about the formation mechanism of α -alumina.

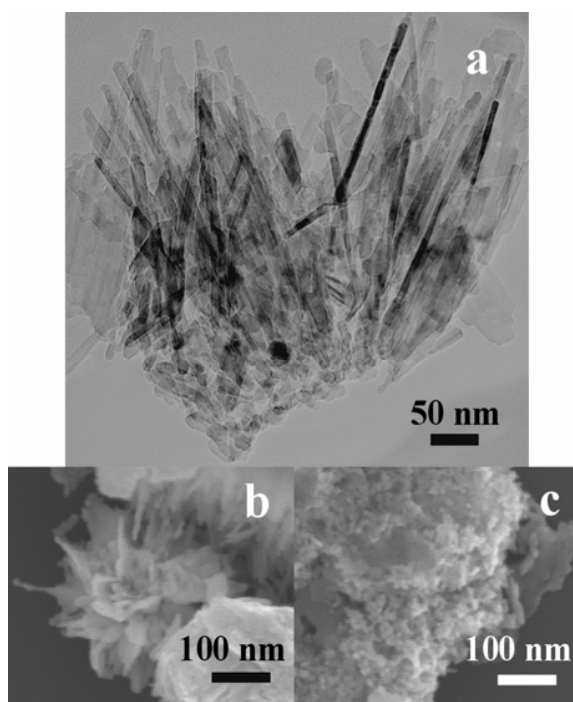


Figure 21 Transmission electron microscopy (TEM) image in (a) and field emission scanning electron microscopy (FESEM) images in (b-c) of the nanocrystalline α -alumina obtained at 1000 °C for 40 h [II].

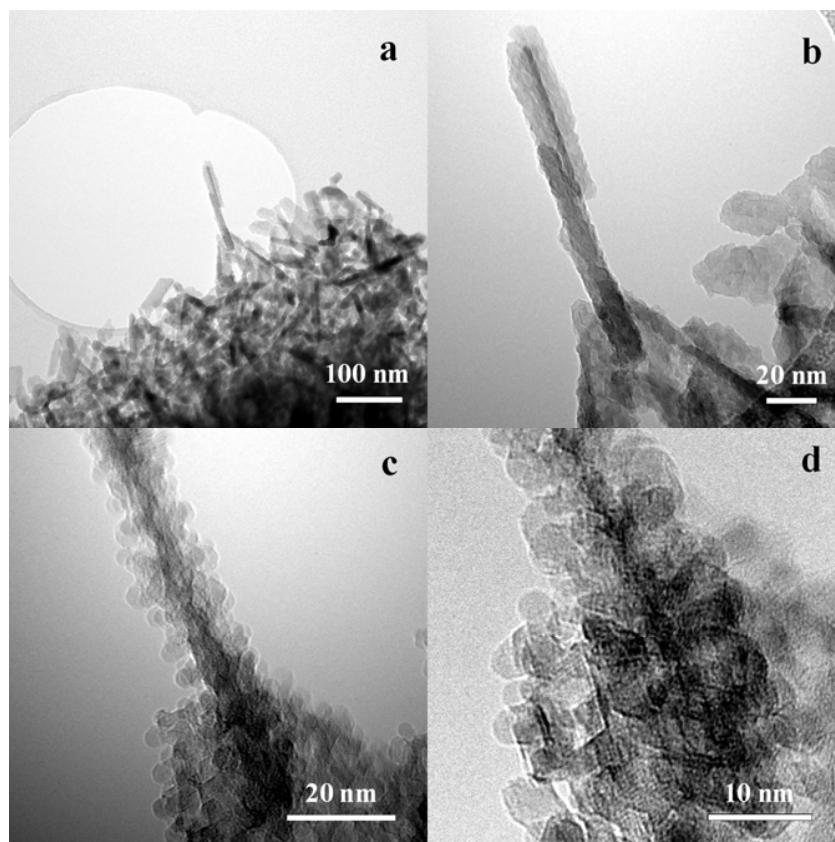


Figure 22 Images of the as-synthesized α -alumina at 1000 °C for 40 h at the same position with increasing magnifications from (a) to (d) [II].

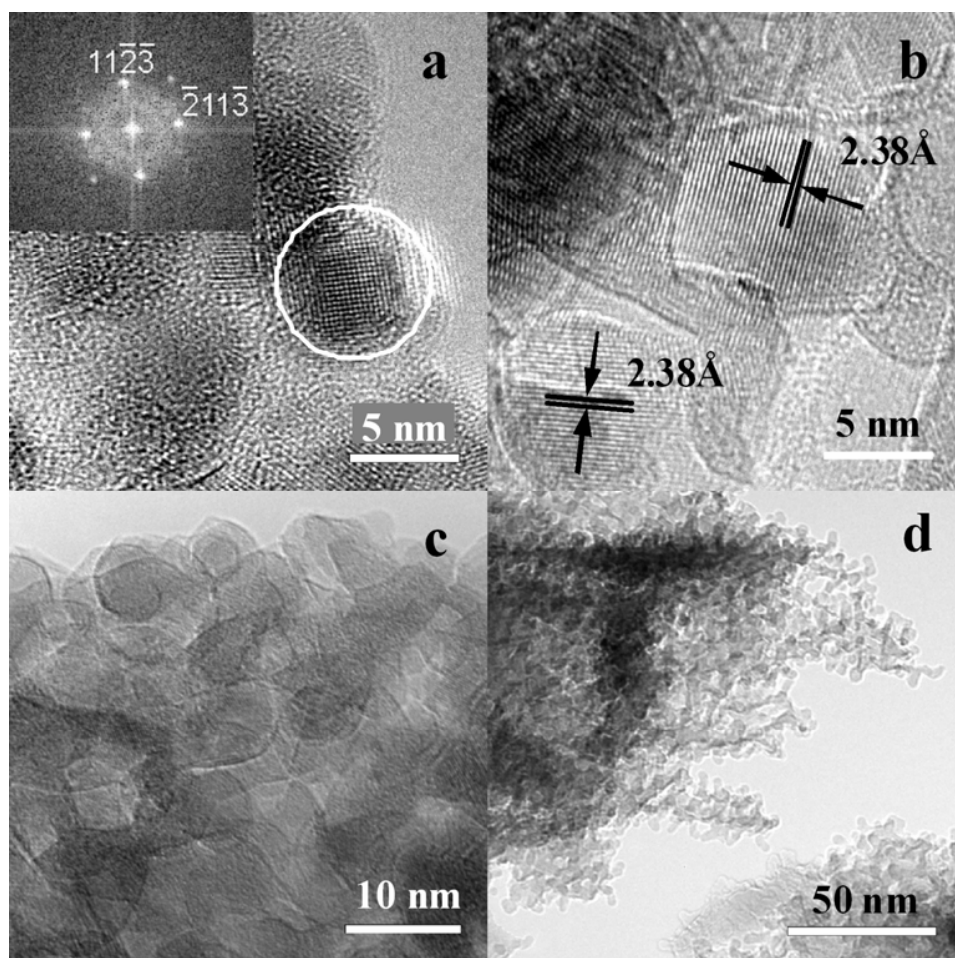


Figure 23 Images of the as-synthesized α -alumina. The corresponding FFT pattern of the circled area is inserted and indexed in (a), in which the beam direction is $[1\bar{2}1]_1$. The calculated plane spacing of 2.38\AA in (b) corresponds to the plane $(11\bar{2}0)$ of α -alumina [II].

4.2.2 Porosity Analysis

The N_2 adsorption/desorption isotherms and pore size distribution curves of the aluminas prepared by calcining the flaky boehmite powder at $1000\text{ }^\circ\text{C}$ from 1 h to 40 h are shown in figure 24. The BET surface areas of the samples are $79\text{ m}^2/\text{g}$ for 1 h, $66\text{ m}^2/\text{g}$ for 5 h, $26\text{ m}^2/\text{g}$ for 20 h, $10\text{ m}^2/\text{g}$ for 30 h and $8.2\text{ m}^2/\text{g}$ for 40 h. All the isotherms are type IV isotherms, which are related to the mesopores in the samples. The hysteresis loops are H2 type for the samples of 1 h and 5 h, which have also micropores indicated from the adsorption at very low relative pressure. This can be also seen from their pore size distribution curves, in which the pore size distributions of both are bimodal with narrow distributions centered on 6 nm and wide distributions from 10 to 100 nm. The pore size distribution around 6 nm is due to the nanocrystalline δ - and θ -alumina, which agrees well with their estimated crystallite sizes d_{XRD} of 5.9 nm for 1 h and 6.6 nm for 5 h. The wide pore size distribution from 10 to 100 nm of the transition alumina for 1 h is mainly from the

interspaces between the transition alumina nanorods (see figure 17). For 5 h, α -alumina started to form, which led to a decrease in the BET surface area and a broadening in the pore size distribution curve. When the dwell time increased to 20 h and 30 h, the amount of α -alumina was increased and θ -alumina grew to a larger d_{XRD} of 13 nm, resulting in a further decrease in the BET surface area and the disappearance of the pore size distribution around 6 nm. However the isotherms still have H2 hysteresis loops, although the hysteresis loop of the sample for 30 h looks very similar with H3 hysteresis loop. When the dwell time was increased to 40 h, the phase transformation to α -alumina was finally completed. The isotherm has a H4 hysteresis loop with a wide distribution of mesopores. H4 hysteresis loop is related with slit-shaped pores [80].

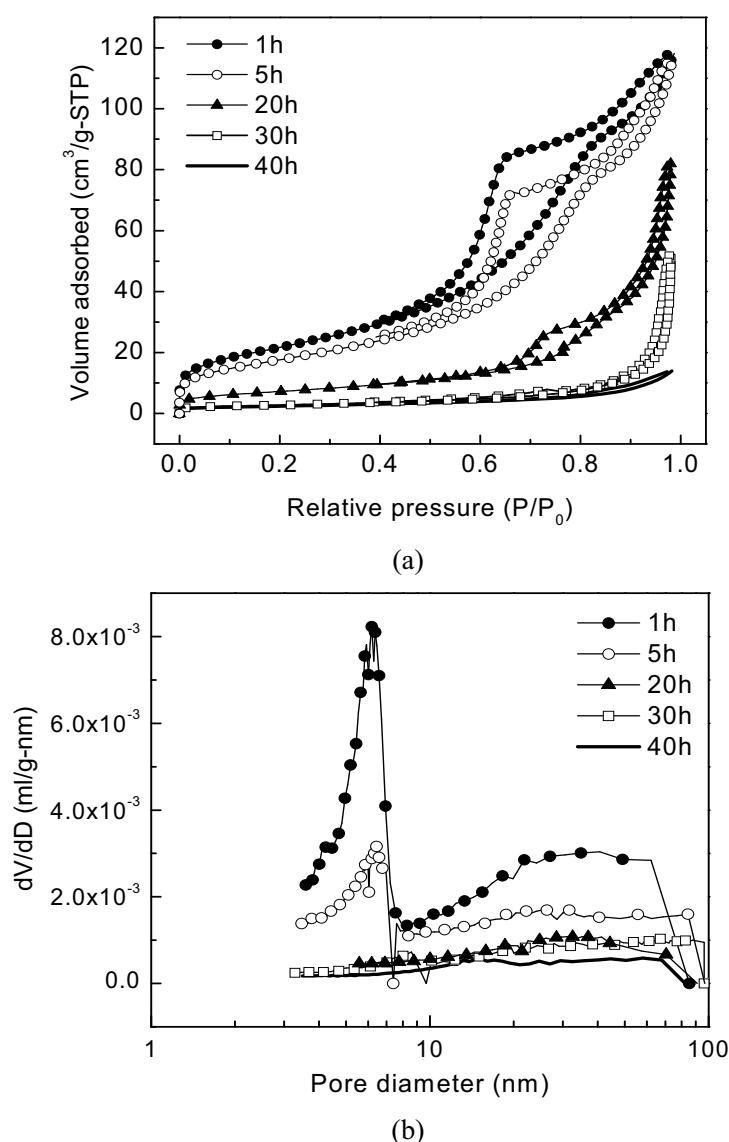


Figure 24 Nitrogen adsorption/desorption isotherms in (a) and the corresponding pore size distribution curves in (b) of the aluminas obtained by calcining the flaky boehmite powder at 1000 °C from 1 h to 40 h [III].

4.2.3 Formation Scheme of the Morphology of the Nanocrystalline α -Alumina

The hypothetical formation scheme of the morphology of the nanocrystalline α -alumina is illustrated in figure 25. The XRD, BET and HRTEM studies of the flaky boehmite powder calcined at 600 °C for 6 h, 1000 °C for 1 h and 1000 °C for 20 h are used to determine the sequence and morphologies of the intermediate phases to form the nanocrystalline α -alumina. The diamonds represent the crystallites of the materials.

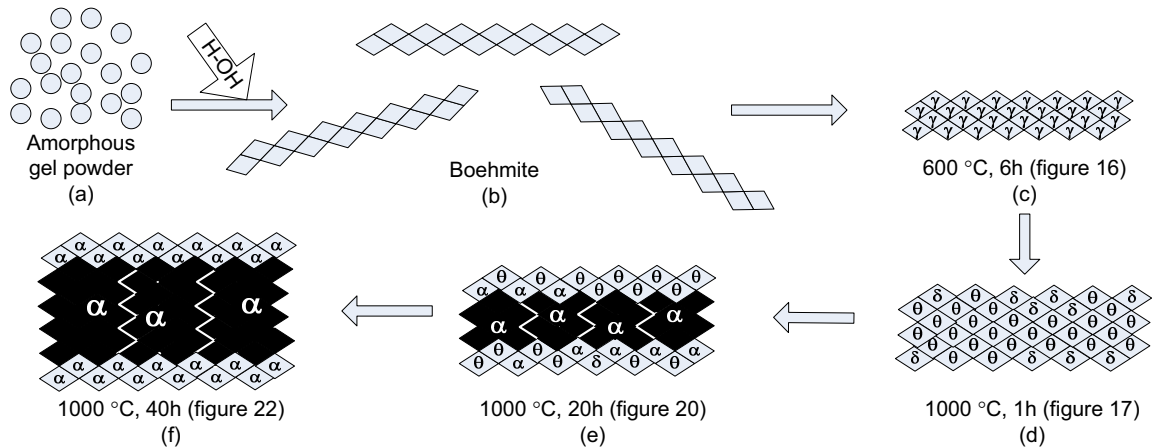


Figure 25 Schematic illustration of the formation of the nanocrystalline α -alumina with novel morphology at 1000 °C for 40 h [III].

The gel powder was of amorphous particles with a high BET surface area of 576 cm²/g. When the gel powder reacted with boiling water, boehmite flakes were formed with the crystallite size d_{XRD} of 3.9 nm. The formation of the flakes resulted from the preferential growth due to the presence of weak hydrogen bonds and the interaction between the solvent molecules and the surface OH⁻ groups via hydrogen bonds [16]. When the flaky boehmite powder was calcined at 600 °C for 6 h, boehmite transformed to γ -alumina with d_{XRD} of 4.0 nm. The γ -alumina crystallites formed into rods with widths of 10 nm and lengths of 300 nm as shown in figure 16. The transformation of boehmite to γ -alumina preserved the morphology of boehmite which is a classical example of a topotactic reaction [85]. When the flaky boehmite powder was calcined at 1000 °C for 1 h, transition aluminas (δ - and θ -alumina, perhaps also γ -alumina) were formed with d_{XRD} of 5.9 nm. The crystallites formed into rods with widths of about 15 nm and lengths of 300 nm. When the boehmite powder was calcined at 1000 °C for 20 h, transition alumina such as θ -alumina was obtained. The 5 nm-crystallites grew into bigger crystallites, as indicated by an evaluated d_{XRD} of 12 nm for θ -alumina, as shown in the black core area in figure 25 (e). The 12 nm-crystallites then formed into large particles and rods. However, the crystallites of 5 nm in size can still be observed in the sample, see figure 20. Finally at 1000 °C for 40 h, boehmite transformed completely into α -alumina where larger rods and particles were formed, however, crystallites of about 5 nm in size can still be observed on the surface of the nanorods and nanoparticles. The evaluated d_{XRD} is 51 nm for the bigger crystallites, as shown in the black

core area in figure 25 (f), which formed into larger particles and rods with particle size d_{BET} of 184 nm.

4.2.4 Phase Transformation of θ - to α -Alumina

When using boehmite as the starting material to form α -alumina, it passes the sequence of γ -, δ -, θ -, and finally α -alumina [10]. The phase transformation between γ -, δ -, θ -alumina are believed to be topotactic and of relatively low energy [21, 85]. However, the phase transformation from θ - to α -alumina involves a change in the oxygen sublattice from cubic to hexagonal close packing and is generally completed at ~ 1200 °C [14]. It is commonly believed that α -alumina is formed by a nucleation and growth mechanism. There are mainly two opinions of the nucleation mechanism from θ -alumina to α -alumina: shear nucleation and diffusional nucleation. The supporters to the shear nucleation mechanism have suggested that the θ -alumina crystallites are ‘sintered’ to a critical size, and then transforms to α -alumina by shear displacement of the oxygen anions [86-87]. The observed critical size of θ -alumina is from 17 nm to several tens of nanometers [27, 32, 87]. Diffusional nucleation of α -alumina has received little attention as compared to the studies that support shear nucleation; however, one major point supporting the diffusional nucleation is the effect of seeds. Many studies have shown that seeds can lower the formation temperature of α -alumina by providing low energy sites for diffusional nucleation and growth [29-31]. Bagwell *et al.* [32] studied the role of ‘critical size’ in the diffusional nucleation and concluded that the ‘critical size’ was not a prerequisite for α -alumina nucleation, but primarily a result of the incubation time required to produce α -alumina nuclei by diffusional nucleation. Bagwell *et al.* [32] also suggested that the reported large α -alumina nuclei was not due to the shear of large θ -alumina crystallites, but was due to the difficulties in detecting small nuclei and the rapid growth of the α -alumina crystallites after nucleation.

In this study, if there is a ‘critical size’ of θ -alumina, it will be 5.9 nm which is possibly the smallest ‘critical size’ observed. However, there is a trend that with the improvement of the characterization methods, it seems that the ‘critical size’ is getting smaller and smaller all the time. Therefore of the two existing mechanisms, the diffusional nucleation mechanism is more consistent in our study. We agree to Bagwell *et al.* that the reported ‘critical size’ is not a must for α -alumina nucleation, but a result of incubation time needed to form α -alumina nuclei by diffusional nucleation. Our study suggests that the 5 nm-crystallites of α -alumina grow into larger crystallites with d_{XRD} of 51 nm which then form into even larger particles and rods with d_{BET} of 184 nm. Therefore when the boehmite powder was calcined at 1000 °C for 40 h, α -alumina crystallites of 5 nm in size can be observed together with larger nanorods and nanoparticles.

4.3 Nanocrystalline α -Alumina at 1000 °C from Gel Powder

By calcining the gel powder, nanocrystalline α -alumina can also be obtained at 1000 °C for 6 h, see figure 26. The amorphous gel powder transformed to α -alumina completely when the dwell time was 6 h.

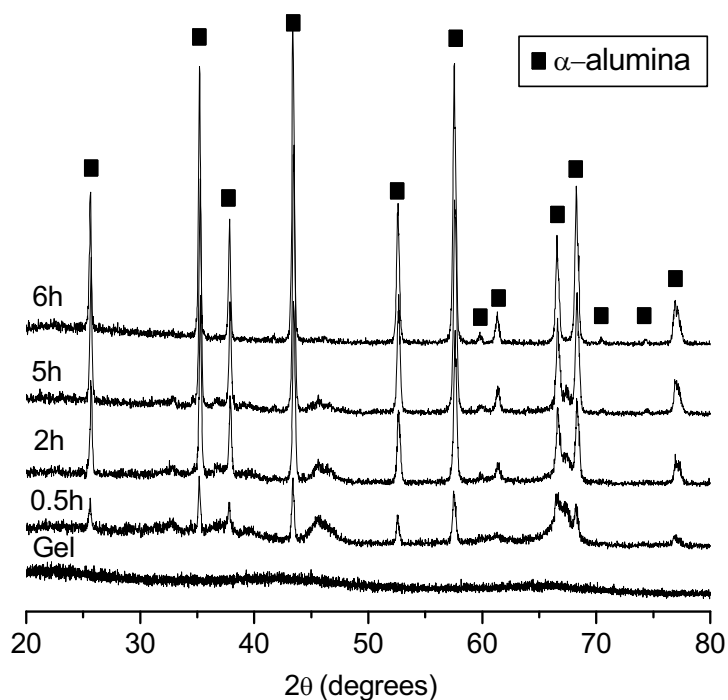


Figure 26 X-ray diffraction (XRD) patterns of the gel powder, and the samples obtained by calcining the gel powder at 1000 °C from 0.5 h to 6 h. The squares signify the diffraction peaks of α -alumina [IV].

The thermal behavior of the gel powder was studied by the TG-DSC curves in figure 27. The gel powder undergoes three stages of decomposition in the TG curve. The first stage under 140 °C is the liberation of the adsorbed water from the pores in the gel powder. The second stage at 140-300 °C corresponds to the removal of the structural water in the gel network and organic residues, while the third stage at 300-500 °C is due to dehydroxylation [88]. The total weight loss is about 60 %. As known, gel transforms to η -alumina, then θ -alumina, and finally α -alumina [10]. Therefore the exothermic peak in the DSC curve around 421 °C could be due to the formation of η -alumina, the peak around 816 °C due to the formation of θ -alumina, and finally the peak around 1100 °C due to the formation of α -alumina.

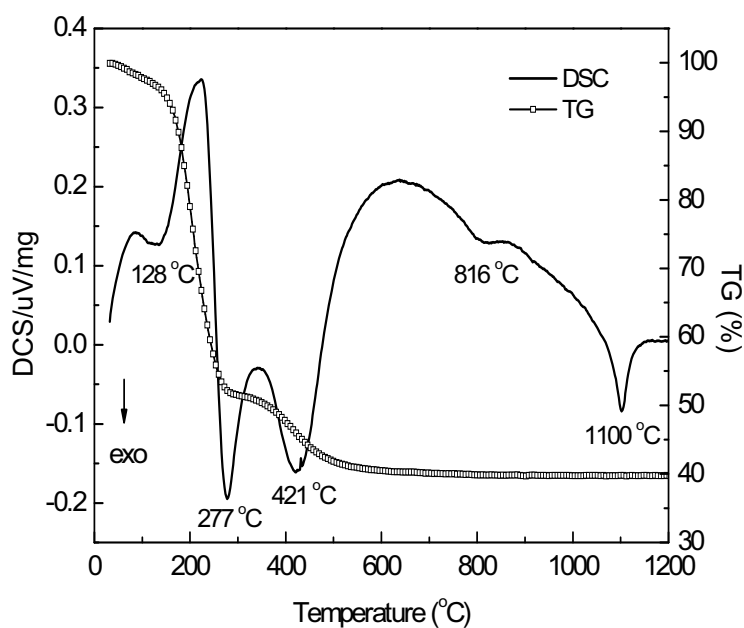


Figure 27 Thermogravimetry-differential scanning calorimetry (TG-DSC) curves of the gel powder [IV].

The morphology of the obtained alumina from the gel powder is shown in figure 28. At 1000 °C for 0.5 h, α -alumina coexisted with transition aluminas (η - and θ -alumina), with a BET surface area of 57 m²/g. Strong agglomeration/aggregation can be seen from figure 28 (a). However, crystallites of 5 nm in size can be clearly observed. When the gel powder was calcined at 1000 °C for 6 h, transition alumina transformed completely to α -alumina with a BET surface area of 5.8 m²/g. The loss in the BET surface area is due to the increased agglomeration/aggregation as well as the transformation from transition alumina to α -alumina and its crystallite growth. Particles of α -alumina with nearly spherical morphology in size of about 100 nm are shown in figure 28 (c). However, small crystallites of α -alumina can be observed, see figure 28 (d).

The schematic illustration of the formation of the nanocrystalline α -alumina in spherical morphology is shown in figure 29. The morphology of the starting material plays a very important role in the morphology of the resulting nanocrystalline α -alumina. The gel powder obtained by drying the sol suspension has a BET surface area of 576 m²/g. The large surface area suggests that the gel powder consists of tiny particles. As known, gel transforms to η -alumina, then θ -alumina, and finally α -alumina [10]. When the gel powder was calcined, η -alumina nanocrystallites were first formed, and then transformed into θ -alumina nanocrystallites which agglomerated into larger particles. Finally α -alumina nanocrystallites were formed at 1000 °C for 6 h, which aggregated into large particles, as shown in figure 28 (c).

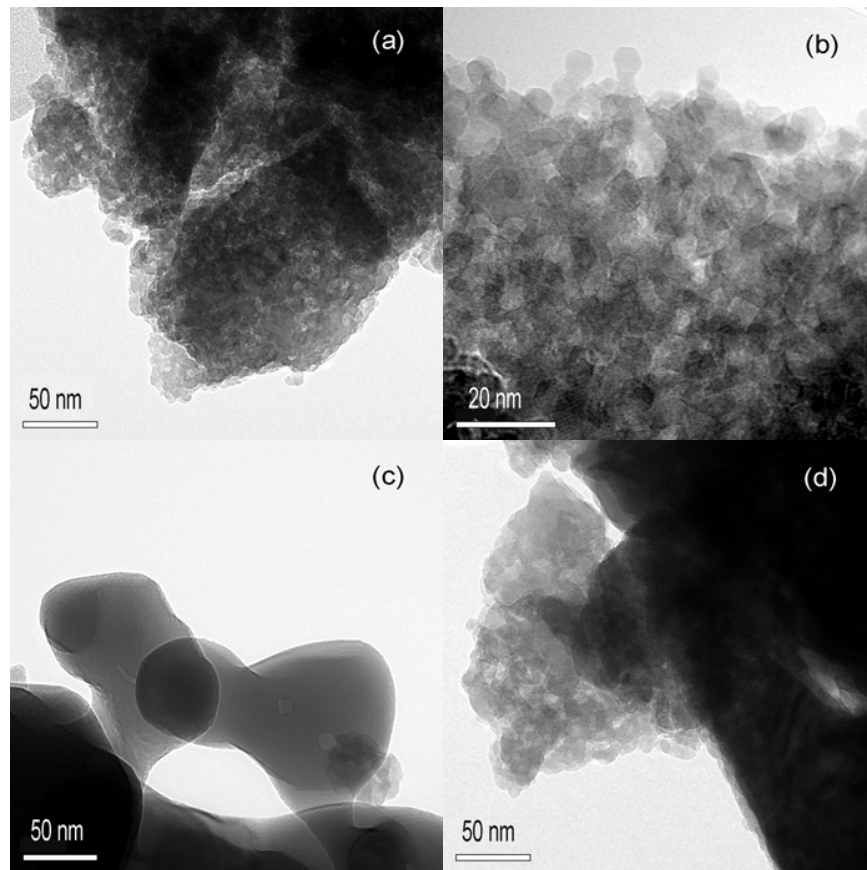


Figure 28 Transmission electron microscopy (TEM) images of the samples obtained by calcining the gel powder for 0.5 h (a-b) and 6 h (c-d) at 1000 °C [IV].

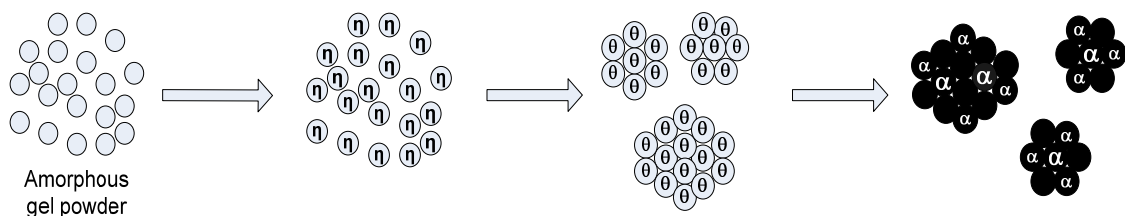


Figure 29 Schematic illustration of the formation of the nanocrystalline α -alumina in spherical morphology from the gel powder [IV].

4.4 Superhydrophobic Flaky Boehmite Film on Stainless Steel

By spin-coating the sol suspension sol B, as indicated in figures 2 and 12, gel film was made on austenitic stainless steel. The gel film was first pre heat-treated, then water boiled, after that post heat-treated, and finally coated with a FAS top layer to obtain the superhydrophobic property. The measured thickness of the FAS layer is 7 nm by depositing only a FAS layer on a bear glass substrate. Therefore the FAS layer modifies the surface energy while following the surface topography of the flaky boehmite film.

4.4.1 Effect of Heat-Treating Gel Film on the Formation of the Flaky Structure of Boehmite

To study the effect of pre heat-treating the gel film on the formation of the superhydrophobic flaky structure of boehmite, the gel film was pre heat-treated at different temperatures from RT to 900 °C for 15 min, then water boiled, and finally FAS treated. The contact angles for water of the as-synthesized films (boiling water treated and FAS treated) obtained from the pre heat-treatments at different temperatures are above 150° between 200 °C and 600 °C, whereas 130° at RT, 144° at 100 °C, 142° at 700 °C, 127° at 800 °C, and 121° at 900 °C. As known, surface energy and surface roughness (i.e. topography) are two dominant factors to obtain superhydrophobic surface. In this study, low surface energy is introduced by the FAS top layer. Contact angles of above 150° for the films between 200 and 600 °C indicate their surface topography to be in an optimized range to trap enough air which reduces the contact area between the surface and the water droplets. However when the contact angle is under 150°, the surface roughness is not in the optimum range for superhydrophobicity.

The FESEM images in figure 30 show the morphologies of the as-synthesized films (boiling water treated and FAS treated). At RT, only a part of the surface was covered with 50-100 nm boehmite flakes after reaction with boiling water, leading to a contact angle of 130°. At 100 °C, the surface was covered completely with the 50-100 nm boehmite flakes, which gave a higher contact angle of 144°. Between 200 and 600 °C, the flakes of 100-200 nm in size led to contact angles to be above 150°. A typical surface image of such film is shown in figure 30 (c). At 700 °C, the surface flakes grew larger and seemed to be more parallel to the substrate, which led to a decrease in the surface roughness and a decrease in the contact angle value to 142°. At 800 °C, flakes of 100-200 nm in size were formed on a part of the surface, leading to a further decrease in the surface roughness and then in the contact angle value to 127°. At 900 °C, flakes were not formed on the surface. Instead, some equiaxed crystals were observed which gave the lowest surface roughness and also the lowest contact angle of 121°.

To study the influence of the pre heat-treatment temperature of the gel film on the formation of the flaky structure of boehmite, the heat-treated gel film from 100 to 900 °C for 15 min before boiling water treatment were observed by FESEM as comparison. Surface flakes were not observed on all the heat-treated gel films, proving that the surface flakes were formed by reacting the gel film with water. The surfaces were smooth for the gel films heat-treated below 700 °C, with a typical image in figure 31 (a), where the gel film was pre heat-treated at 600 °C for 15 min. Particulates were not observed on the surface, but some pores could be seen. However, at 700 °C, some particulates of about 50 nm showed up on the surface. At 800 °C, the particles grew larger to 100-200 nm. At 900 °C, the surface was full of the equiaxed crystals of about 200 nm in size.

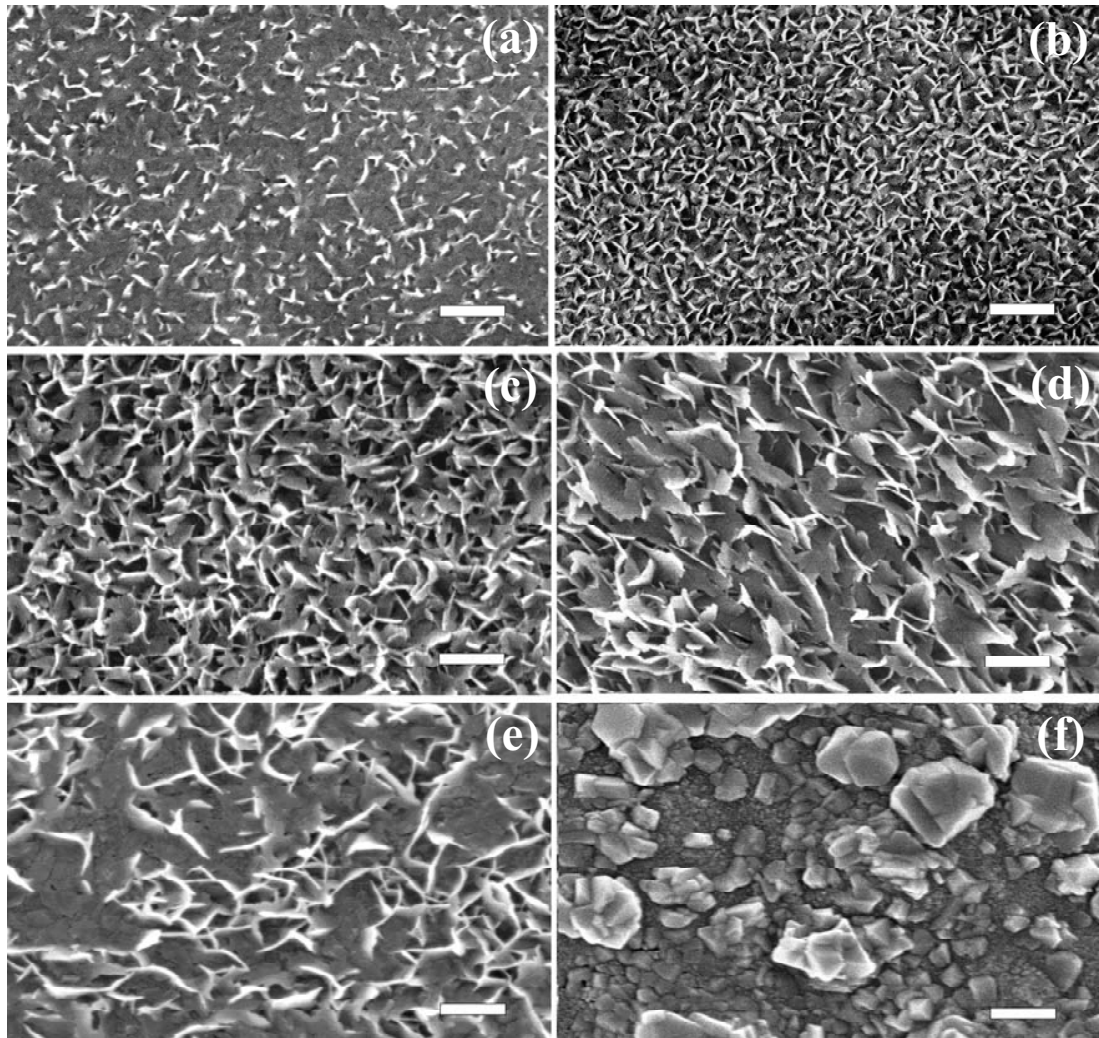


Figure 30 Surface FESEM images of the as-synthesized films (boiling water treated and FAS treated) obtained from the pre heat-treatment at RT in (a), 100 °C in (b) , 400 °C in (c), 700 °C in (d), 800 °C in (e) and 900 °C in (f) for 15 min. Bars = 200 nm [V].

It is supposed that at RT and 100 °C the films were still in the gel state. When the gel films were heat-treated from 200 to 600 °C, amorphous and nanocrystalline η -alumina was formed with the increase of the heat-treatment temperatures. When η -alumina was upon contact with boiling water, boehmite formed on the surface of η -alumina. The Al atoms in the boehmite lattice formed a deformed octahedron with four oxygen and two hydroxide neighbors. Such octahedron joined by edges resulted in AlOOH polymeric layers. These layers were held together by hydrogen bonds between the OH^- groups of each octahedron [13]. Therefore boehmite had a preferential growth direction due to the presence of weak hydrogen bonds and the interaction between the solvent molecules and the surface OH^- groups via the hydrogen bonds [16]. The above explains the formation of boehmite flakes on the surface of the amorphous and nanocrystalline η -alumina formed from 200 to 600 °C.

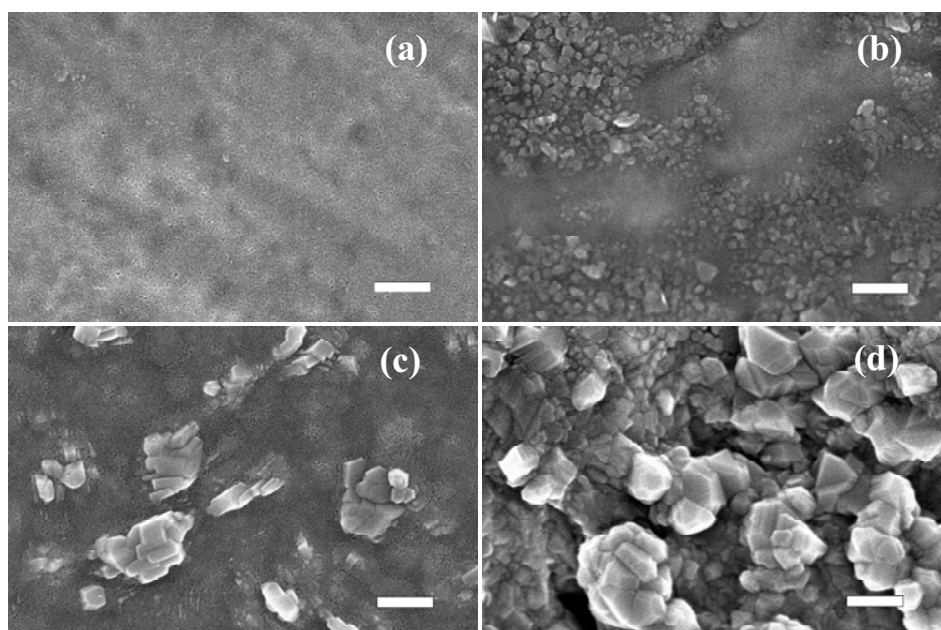


Figure 31 Surface FESEM images of the gel films pre heat-treated at 600 °C in (a), 700 °C in (b), 800 °C in (c) and 900 °C in (d) for 15 min before the boiling water treatment. Bars = 200 nm [V].

The TEM study confirms that formation of nanocrystalline η -alumina, as shown in figure 32 (a). The gel film on the steel disc was heat-treated at 600 °C for 15 min, and then observed under TEM. The SAED pattern was taken from the edge area of the central hole of the disk. The rings in the SAED pattern reveal the formation of nanocrystalline η -alumina. The particles in the bottom of the image are from the stainless steel substrate. When the gel films were heat-treated at higher temperatures, η -alumina was more and more crystallized and η -alumina crystals might be difficult to react with water and might need much longer time to react with water to form boehmite flakes. At 800 °C, some η -alumina crystals showed up, which led to the formation of poorly-shaped flaky structure of boehmite after immersed into boiling water for 10 min. And at 900 °C, the gel film was full of equiaxed η -alumina crystals which did not react with water with an immersing time of 10 min. This could explain the similarity of the FESEM images in figure 30 (f) and figure 31 (d). A gel film on steel disk was heat-treated at 900 °C for 15 min, and studied under TEM, see figure 32 (b). Then the disk sample was reacted with boiling water for 10 min, and studied again under TEM, see figure 32 (c). Flakes were not observed at all under TEM either before or after the water treatment in figure 32 (b) and (c). The SAED pattern of the gel film pre heat-treated at 900 °C was indexed according to η -alumina with a beam direction of [011], as shown in figure 32 (b). The particle size agrees well with the FESEM image in figure 31 (d). And after the boiling water treatment, the SAED pattern was indexed to be η -alumina with a beam directions of $[\bar{1}12]$ as shown in figure 32 (c), which could indicate that the η -alumina crystals did not react with water. As stated in chapter 2, η -alumina and γ -alumina have very similar XRD data, therefore it is very difficult to

conclude whether η -alumina was formed or γ -alumina was formed by the SAED patterns. The formation of η -alumina is speculated since the gel film was the starting material for the heat-treatment.

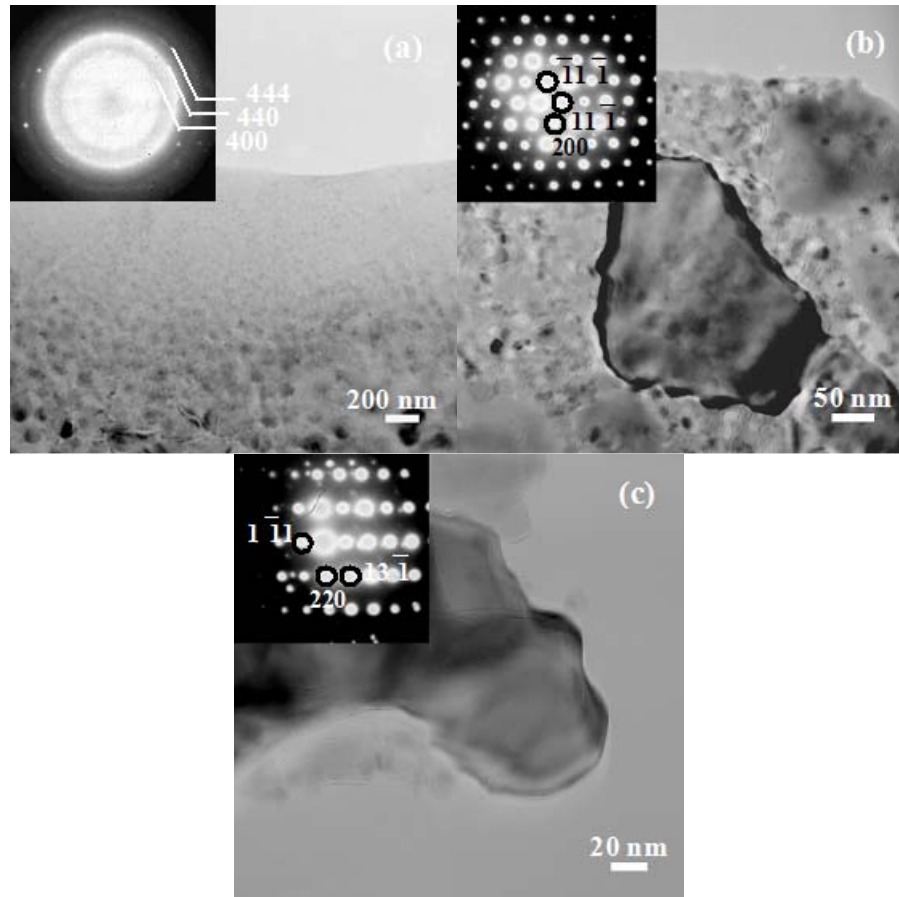


Figure 32 Typical TEM images of the gel film on the steel disk heat-treated at 600 °C (a) and 900 °C (b). The TEM image in (c) was taken after the disk sample in (b) reacted with boiling water. The SAED pattern in (a) was taken from the edge area, and the SAED patterns in (b) and (c) were from the corresponding crystallites on the images. The SAED patterns were indexed according to η -alumina with beam directions of $[011]$ in (b) and $[\bar{1}12]$ in (c) [V].

4.4.2 Thermal Stability of the Flaky Surface Structure

As known, typically many superhydrophobic surfaces suffer from weak wear resistance. A high temperature treatment would form oxide from hydroxide and remove water, which could improve the mechanical properties and resistance of the surface. For this purpose, thermal stability of such nanoscale flaky surface structure was studied to find out the temperature range in which such nanoscale surface structure can be retained so that the surface can remain to be superhydrophobic.

To fulfill this purpose, the gel film was pre heat-treated at 400 °C for 15 min, then water boiled, after that post heat-treated from 100 to 900 °C for 30 min and finally FAS treated.

With the post heat-treatments from 100 to 600 °C, the contact angle values for water were above 150°, which indicated that the surface had a sufficient roughness for the superhydrophobicity. However, when the temperature was further increased, the contact angle for water dropped to 139° at 700 °C, 132° at 800 °C and 129° at 900 °C. This is due to the loss of the surface roughness during the post heat-treatments. The more surface roughness loses its micro/nano details, the more contact angle decreases. The surface of the post heat-treated films can be seen in figure 33. When the film was post heat-treated at 700 °C, a part of the flaky structure on the surface changed the morphology to coarser flakes and the surface lost the roughness to some extent, see figure 33 (a). When increasing the temperature to 800 °C, more flake structure changed the morphology to well-shaped crystals, as shown in figure 33 (b), leading to a further decrease in the contact angle value. At 900 °C, almost all the surface flakes were changed into equiaxed crystals in size of around 100 nm as shown in figure 33 (c). However, there were still few flakes left on the surface.

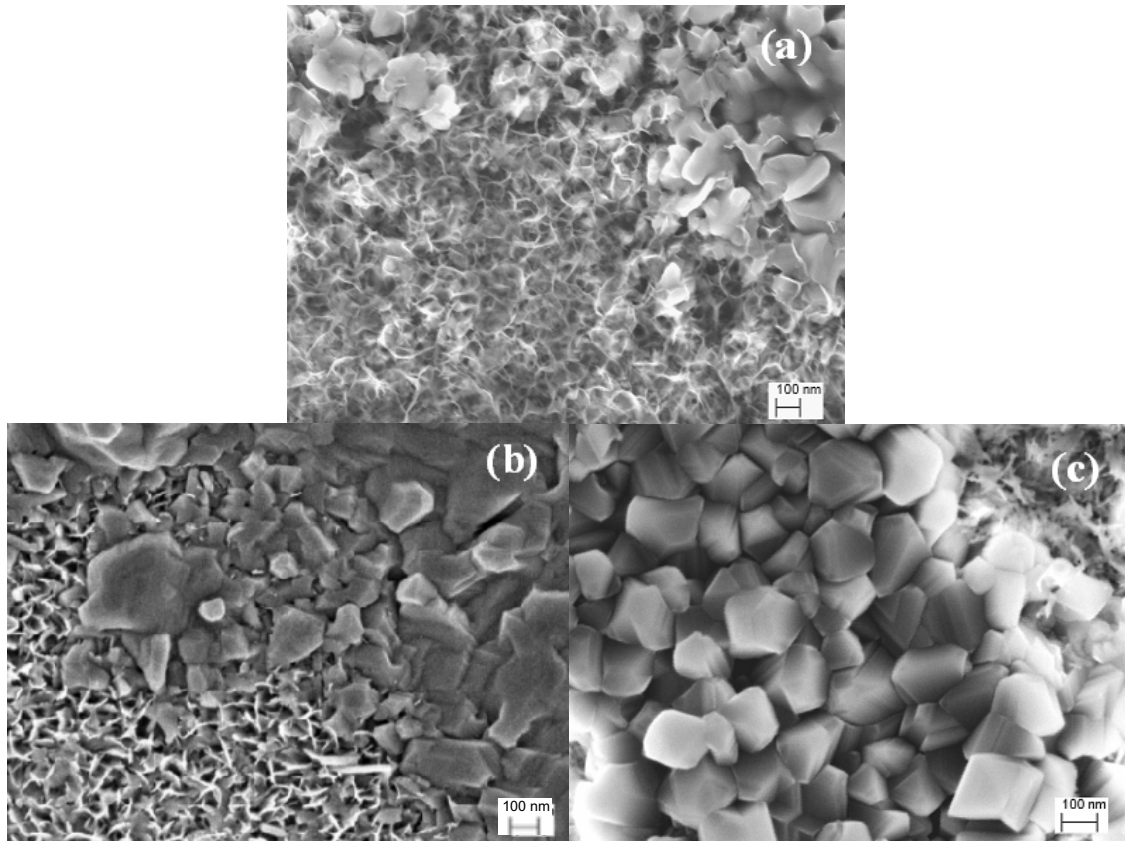


Figure 33 Field emission scanning electron microscopy (FESEM) surface images of the boehmite films post heat-treated at 700 °C in (a), 800 °C in (b) and 900 °C in (c) for 30 min. Bars = 100 nm [VI].

To find out what is the crystalline phase formed during the post heat-treatment, TEM study was carried out. The TEM images of the boehmite film made on steel disk post heat-treated at 900 °C are given in figure 34, where the indexed SAED patterns of the circled crystallites

are also inserted. The size of the crystallites in figure 34 is around 100-150 nm, which is in good agreement with the crystallite size shown in the FESEM image in figure 33 (c). All three SAED patterns are assigned to γ -alumina and the beam direction is $[\bar{1}11]$ in (a), $[\bar{1}12]$ in (b) and $[011]$ in (c).

At 600 °C, boehmite should already transform to γ -alumina based on the study in previous sections. However, the formation of the γ -alumina at 600 °C did not change the surface roughness much, and the surface roughness was still sufficient to retain the superhydrophobic property. Therefore the flaky boehmite film can be post heat-treated at 600 °C for 30 min to improve the wear resistance of the film, while retaining the superhydrophobicity. The wear resistance of the post heat-treated film is under study. Above 700 °C, more and more γ -alumina was formed, accompanied with a more considerable change in the surface roughness, which further decreased the contact angle value. At 900 °C, most of the boehmite was changed into well-crystallized γ -alumina, as shown in figures 33 (c) and 34. It is possible that some δ -alumina even some θ -alumina remained in the sample, however, they were not observed in the TEM study.

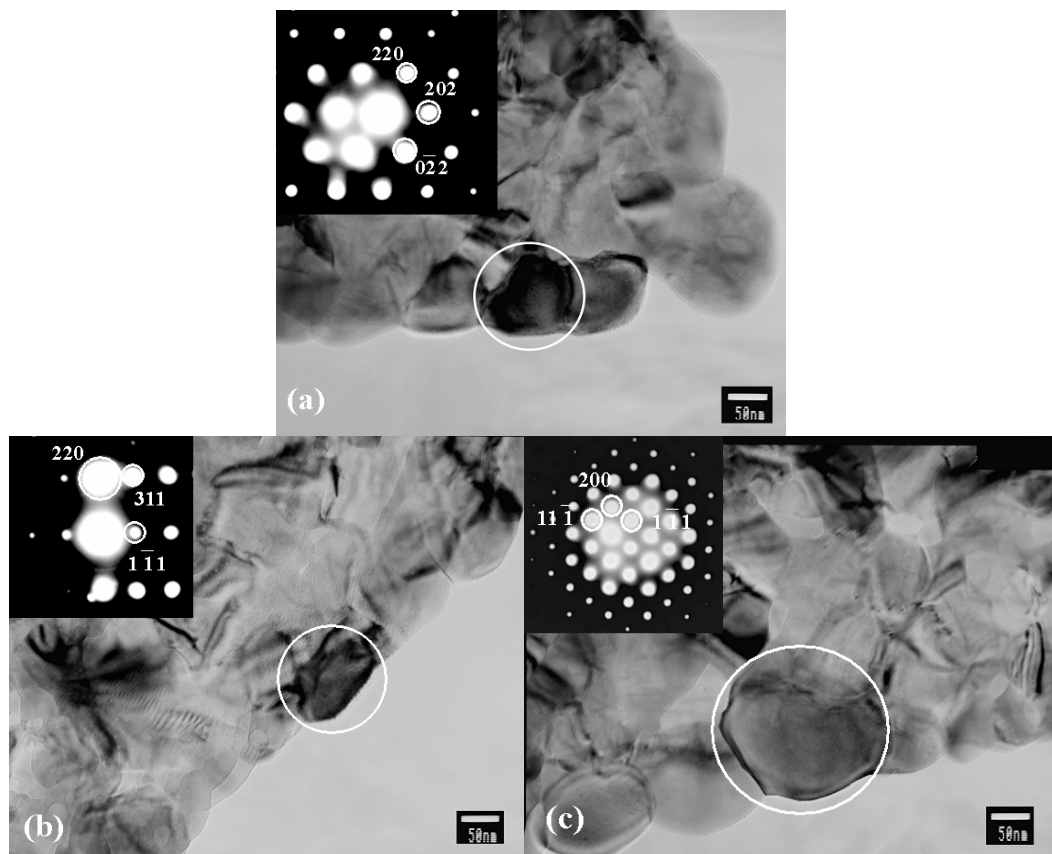


Figure 34 Transmission electron microscopy (TEM) images of the boehmite film on steel disk post heat-treated at 900 °C. The corresponding SAED patterns obtained from the circled crystallites are inserted. Beam direction is $[\bar{1}11]$ in (a), $[\bar{1}12]$ in (b) and $[011]$ in (c) [VI].

4.5 Superhydrophobic Antireflective Boehmite Film on Glass

The superhydrophobic antireflective boehmite films with different topographies were made by varying the heat-treatment temperatures. With different topographies the films show different optical transmittances and contact angles. The specimens marked as A1-100, A1-300 and A1-500 were made from sol A by spin coating at 1500 rpm for 20 s on the microscope glass slides. The samples were then heat-treated at 100, 300 and 500 °C as denoted in the code in air for 15 min. After cooling down, the films were treated with boiling water and after that they were treated by FAS. By using the same heat-treatment temperature of 300 °C, B1-300 and B2-300 were made from sol B with different amount of gel layers (1 and 2 layers) as indicated in the sample names. In B2-300, after depositing the first gel layer, heat-treatment at 400 °C for 30 min was carried out. Then a second gel layer was made. After that, heat-treatment at 300 °C, boiling water treatment and FAS treatment were done.

The optical transmittance spectra of A1-100, A1-300 and A1-500 are given in figure 35, in which the optical transmittance of the reference glass is also given. The optical transmittances of all the three films are better than that of the reference glass. Sample A1-100 has the smallest increment in optical transmittance and sample A1-300 has the highest. The high optical transmittance is over a broad bandwidth from 350 to 900 nm, which could be called broadband antireflective property.

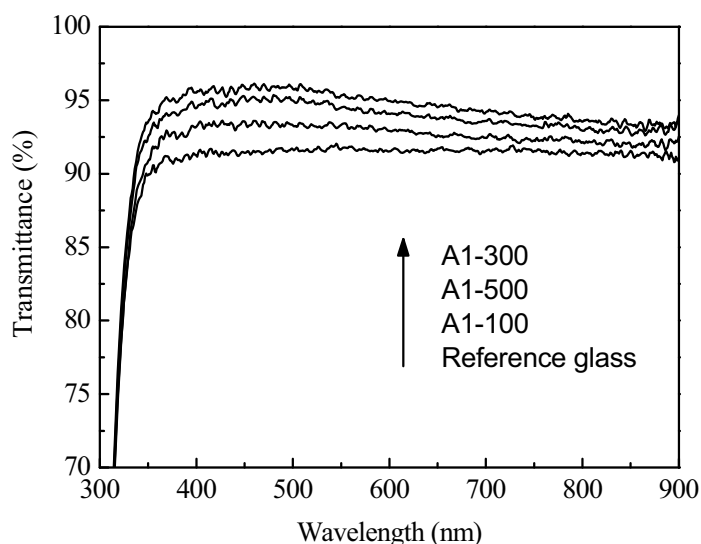


Figure 35 Optical transmittance spectra of the reference glass substrate, and of the film samples A1-100, A1-500 and A1-300 [VII].

When varying the thickness of the gel film by using different sol suspensions and spin coating different layers, optical transmittances of the heat-treated, boiling water treated and FAS treated films are also different. Typical cross-sectional FESEM images of the films

A1-300, B1-300 and B2-300 are given in figure 36. The film thickness of A1-300 is about 170 nm, of B1-300 about 230 nm and of B2-300 about 320 nm. For A1-300 in figure 36 (a), a thin layer of Pt/Pd had to be coated for the imaging process which makes the glass substrate look different with those in figure 36 (b) and (c). The pores in A1-300 and B1-300 are open down to the glass substrate, while in B2-300 there is a more dense layer between the porous surface layer and the glass substrate.

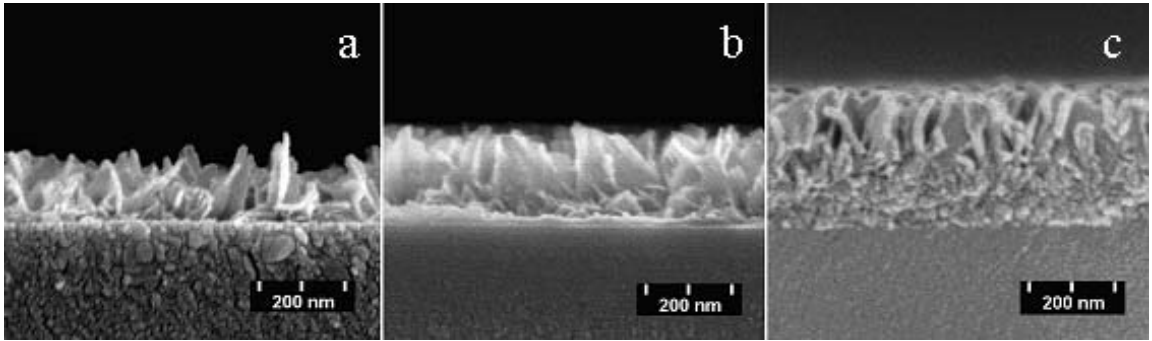


Figure 36 Cross-sectional FESEM images of the film samples A1-300 in (a), B1-300 in (b) and B2-300 in (c) [VII].

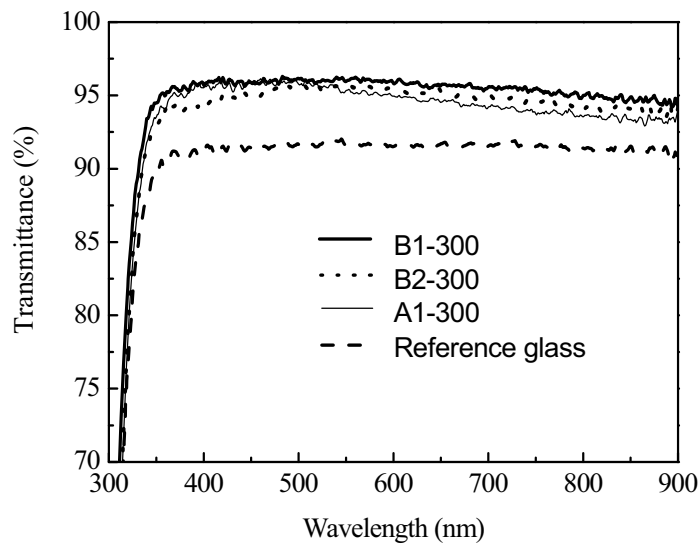


Figure 37 Optical transmittance spectra of the reference glass substrate, and of the film samples B1-300, B2-300 and A1-300 [VII].

The optical transmittances of the three films A1-300, B1-300 and B2-300 are shown in figure 37. When the wavelength is below 520 nm, A1-300 has a slightly better optical transmittance than B2-300. When the wavelength is above 520 nm, B2-300 has a slightly higher optical transmittance than A1-300. However B1-300 has the best optical transmittance over the whole wavelength range with the highest optical transmittance ranging between 95-96 %. Furthermore, the cutting edge of the optical transmission spectrum of B1-300 is lower than that of the reference glass, which broadens the wavelength range with high optical transmittance.

The contact angles for water of A1-100, A1-300, A1-500, B1-300 and B2-300 are 103° , 152° , 152° , 154° and 154° (θ in table 3). Typical AFM images of A1-100, A1-300 and A1-500 and the shape of the water droplets on the surfaces are shown in figure 38. The roughness parameters of the films are given in table 3. The increment in effective surface area S_{dr} is significant for A1-300, A1-500, B1-300 and B2-300 as compared to A1-100. This is the reason of the superhydrophobic behavior of A1-300, A1-500, B1-300 and B2-300. Air can be entrapped in the voids, which leads to a decrease in the contact area between the water droplet and the surface, i.e. the droplet is in the Cassie-Baxter model (equation 3 in chapter 2). The water contact angle of 103° on sample A1-100 indicates that the droplet on this surface is more in the Wenzel state (equation 2 in chapter 2), i.e. water fills the grooves. Also the higher root-mean-square values of the surface slope, S_{dq} , and the mean summit curvature S_{sc} , of A1-300, A1-500, B1-300 and B2-300 indicate the surface with sharp peaks. This means that the contact area between the water droplet and the surface is very small, and that the proportion of air below the droplet is large (larger f_2 value in equation 3 in chapter 2).

Table 3 Measured water contact angles and roughness parameters of the film samples A1-100, A1-300, A1-500, A2-300 and B2-300 [VII].

	A1-100	A1-300	A1-500	B1-300	B2-300
θ ($^\circ$)	103	152	152	154	154
S_{dr} [%]	2.5	71.7	46.1	97.8	24.2
S_{dq} [1/nm]	0.2	1.3	1.1	1.6	0.7
S_{sc} [1/nm]	$4.7 \cdot 10^{-4}$	$3.9 \cdot 10^{-3}$	$2.7 \cdot 10^{-3}$	$6.3 \cdot 10^{-3}$	$2.6 \cdot 10^{-3}$
S_q [nm]	2.7	28.1	16.0	27.6	13.8
S_{sk}	0.52	0.07	0.28	-0.12	0.13

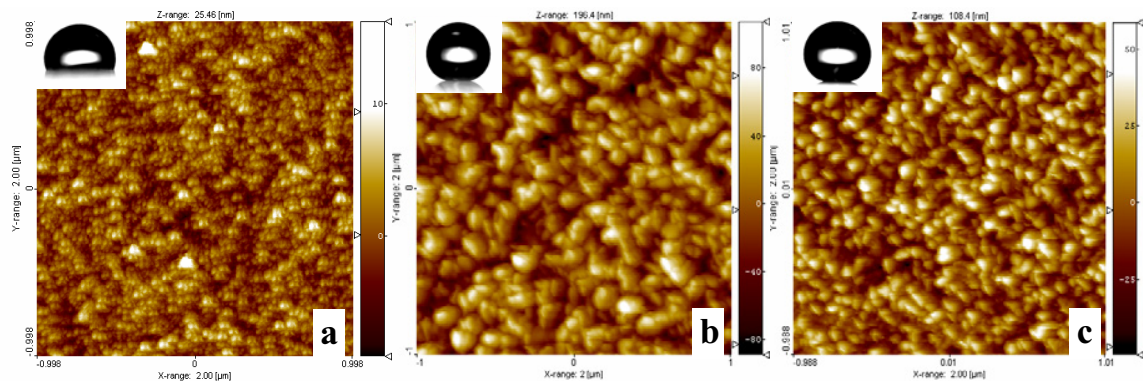


Figure 38 Atomic force microscopy (AFM) images ($2 \times 2 \mu\text{m}$) of A1-100 with z range of 25 nm in (a), A1-300 with z range of 196 nm in (b) and A1-500 with z range of 108 nm in (c) [VII].

It seems that there is also a good correlation between the optical transmittance and the roughness parameters. Of the samples A1-100, A1-300 and A1-500, A1-300, which gives the best optical transmittance, has the highest root-mean-square roughness value S_q while A1-100, which gives the least increment in optical transmittance, has the lowest S_q . And the optical transmittance and S_q of A1-500 are both in between. The skewness value S_{sk} describes the asymmetry of the height distribution. A1-300, with the smallest S_{sk} value, can be described as the sample least dominated by surface summits (peaks), which seems to give the best optical transmittance. While A1-100 with the highest S_{sk} value gives the lowest increment in optical transmittance. The optical transmittance seems also to correlate with the hybrid parameters S_{sc} and S_{dq} . The higher values of S_{sc} and S_{dq} seem to give better transmittance. The differences of S_{sc} and S_{dq} between samples A1-300 and A1-500, however, are fairly small, too small to unambiguously explain the differences in optical characteristics between these two samples. On the other hand, of the samples A1-300, B1-300 and B2-300, B1-300 is the only film with a negative S_{sk} skewness value, which indicates that the surface becomes slightly dominated by valleys. For both A1-300 and B2-300 the skewness value is positive, i.e. the surface is dominated by peaks rather than valleys. The difference in the skewness values seems at least partly to explain the optical behavior of the samples – sample B1-300, the only sample with a negative skewness value, shows the best optical transmittance. The S_q values of A1-300 and B1-300, and S_{sc} and S_{dq} values of all three films are quite close. Although it seems that higher values of S_q , S_{sc} and S_{dq} relate to higher optical transmittance, it is difficult to draw unambiguous conclusions.

5. CONCLUDING REMARKS AND SUGGESTIONS FOR FUTURE WORK

In this dissertation, synthesis, characterization and applications of nanocrystalline functional alumina (Al_2O_3) and boehmite ($\gamma\text{-AlOOH}$) materials have been systematically studied. Based on the same sol suspension made from the sol-gel technique, gel powder and gel film was obtained. By reacting the gel powder and the gel film with boiling water, flaky boehmite powder and film was prepared. By calcining the flaky boehmite powder and film, alumina powder and film was synthesized. The results and conclusions are summarized as following:

- (1) Nanocrystalline flaky boehmite powder with high surface area was synthesized by a simple process, in which gel powder was reacted with boiling water. By calcining the flaky boehmite powder from 500 to 900 °C, nanocrystalline transition aluminas with high surface areas were obtained, showing the morphologies of nanoparticles and nanorods.
- (2) By calcining the boehmite powder at 1000 °C for 1 h, transition aluminas were formed with the morphology of nanorods. When calcining the boehmite powder for 5 h, α -alumina co-existed with transition aluminas, and for 40 h, boehmite was transformed to α -alumina completely. The α -alumina had novel morphology, in which the crystallites of α -alumina in size of 5 nm were observed for the first time, moreover, the phenomenon of the 5 nm-crystallites existing on the surface of nanorods was not reported before. Besides the novel morphology, such nanocrystalline α -alumina was synthesized at a relatively low temperature of 1000 °C though seeding additives were not used. And the nanocrystalline α -alumina (also the transition alumina) was obtained without the use of any structure-directing reagents such as surfactants, which could easily cause collapse of the structure during the removal step.
- (3) We proposed that the morphology of the flaky boehmite powder played an important role on the formation of the novel morphology of the nanocrystalline α -alumina. From the flaky boehmite powder, when increasing the calcining temperature, γ -, δ -, θ - and α -alumina with morphologies of nanorods were obtained, accompanied with crystallite growth. The crystallites of 5 nm can be found on the surface of both the transition alumina and the α -alumina nanorods.
- (4) The phase transformation of θ - to α -alumina was tentatively discussed. In our study, we found that the diffusional nucleation mechanism was more consistent. Our results

support that the reported ‘critical size’ is not a must for α -alumina nucleation, but a result of incubation time needed to form α -alumina nuclei by diffusional nucleation.

- (5) Nanocrystalline α -alumina was also obtained by calcining the amorphous gel powder. However, it had nearly spherical morphology with strong aggregation. This indicated that the flaky boehmite powder was a must to synthesize the nanocrystalline α -alumina with the aforehand-mentioned novel morphology.
- (6) The FAS treated flaky boehmite film was superhydrophobic and antireflective. When the gel film was pre heat-treated between 200 to 600 °C, the flaky structure of the boehmite film could be produced by reacting the gel film with boiling water. The flaky morphology could be retained up to a post heat-treatment of 600 °C, at which boehmite transformed to γ -alumina. Therefore, with the post heat-treatment at 600 °C, it is possible to have improved wear resistance of the surface while retaining the superhydrophobicity.
- (7) The roughness parameters determined by AFM were found to correlate to the superhydrophobicity and antireflectivity. The superhydrophobic property could be related to a high S_{dr} value and the antireflective property to a low S_{sk} value (preferentially negative values) and perhaps also high S_q , S_{sc} , S_{dq} values. This could open a new way to characterize the optical transmittance of the surface.

Based on the results and discussion presented in this dissertation, the following points could be considered for future work:

- a. The stability of the 5 nm-crystallites of the nanocrystalline α -alumina should be found out. Nanomaterials have high surface areas and are very active, thus the 5 nm-crystallites may not remain stable in a long run. The formation temperature of the nanocrystalline α -alumina also needs efforts to be further lowered.
- b. The whole process can be modified to produce alumina supported Fe, Ni, Co catalysts, which can be used to synthesize carbon nanotubes (CNT) by catalytic decomposition of hydrocarbons, for example methane.
- c. Antibacterial behavior of the superhydrophobic film can be studied. Wettability is critical for the adhesion of microorganisms to the surface. Due to the reduced contact area between the bacteria and the surface, the bacteria may not adhere easily to the surface. Meanwhile, on water repellent surface, spore and conidia are lack of water necessarily for germination.

- d. Wear test of the flaky boehmite film and the post heat-treated boehmite film at 600 °C should be carried out to understand more about its durability in order to apply the film in practice. Only when knowing how durable the film is, suitable applications of such flaky film can be found.
- e. The antireflective flaky boehmite film should be studied in solar cell applications. Due to the broadband antireflectivity, it could give higher energy efficiency.

REFERENCES

- [1] R. Brooker and E. Boysen, *Nanotechnology for Dummies*, Wiley Publishing, Inc. Indianapolis, Indiana, 2005
- [2] C. J. Murphy, Materials Science: Nanocubes and Nanoboxes, *Science* **298**, 2002, 2139-2141
- [3] R. Corriu, A. Mehdi and C. Reye, Nanoporous Materials: a Good Opportunity for Nanosciences, *Journal of Organometallic Chemistry* **689**, 2004, 4437-4450
- [4] A. R. Harutyunya, B. K. Pradhan, U. J. Kim, G. Chen and P. C. Eklund, CVD Synthesis of Single Wall Carbon Nanotubes under "Soft" Conditions, *Nano Letters* **2**, 2002, 525-530
- [5] M. Leskelä, M. Kemell, K. Kukli, V. Pore, E. Santala, M. Ritala and J. Lu, Exploitation of Atomic Layer Deposition for Nanostructured Materials, *Materials Science and Engineering C* **27**, 2007, 1504-1508
- [6] M. Niederberger, Nonaqueous Sol-Gel Routes to Metal Oxide Nanoparticles, *Accounts of Chemical Research* **40**, 2007, 793-800
- [7] M. Lazzari, C. Rodriguez-Abreu, J. Rivas and M. A. Lopez-Quintela, Self-Assembly: a Minimalist Route to the Fabrication of Nanomaterials, *Journal of Nanoscience and Nanotechnology* **6**, 2006, 892-905
- [8] C. S. Wang, S. K. Friedlander and L. Mädler, Nanoparticle Aerosol Science and Technology: an Overview, *China Particuology* **3**, 2005, 243-254
- [9] F. Cansell, C. Aymonier and A. Loppinet-Serani, Review on Materials Science and Supercritical Fluids, *Current Opinion in Solid State and Materials Science* **7**, 2003, 331-340
- [10] L. D. Hart, *Alumina Chemicals: Science and Technology Handbook*, The American Ceramic Society Inc, Westerville, Ohio, 1990
- [11] I. Levin and D. Brandon, Metastable Alumina Polymorphs: Crystal Structures and Transition Sequences, *Journal of the American Ceramic Society* **81**, 1998, 1995-2012
- [12] J. Li, Y. Wu, Y. Pan, W. Liu, Y. Zhu and J. Guo, Agglomeration of α -Alumina Powders Prepared by Gel Combustion, *Ceramics International* **34**, 2008, 1539-1542
- [13] A. F. Popa, S. Rossignol and C. Kappenstein, Ordered Structure and Preferred Orientation of Boehmite Films Prepared by the Sol-Gel Method, *Journal of Non-Crystalline Solids* **306**, 2002, 169-174
- [14] H. J. Youn and K. S. Hong, Low-Temperature Formation of α -Alumina by Doping of an Alumina-Sol, *Journal of Colloid and Interface Science* **211**, 1999, 110-113

- [15] P. S. Santos, H. S. Santos and S. P. Toledo, Standard Transition Aluminas: Electron Microscopy Studies, *Materials Research* **3**, 2000, 104-114
- [16] S. C. Kuiry, E. Megen, S. D. Patil, S. A. Deshpande and S. Seal, Solution-Based Chemical Synthesis of Boehmite Nanofibers and Alumina Nanorods, *Journal of Physical Chemistry B* **109**, 2005, 3868-3872
- [17] M. Thiruchitrambalam, V. R. Palkar and V. Gopinathan, Hydrolysis of Aluminium Metal and Sol-Gel Processing of Nano Alumina, *Materials Letters* **58**, 2004, 3063-3066
- [18] Y. Liu, D. Ma, X. Han, X. Bao, W. Frandsen, D. Wang and D. Su, Hydrothermal Synthesis of Microscale Boehmite and Gamma Nanoleaves Alumina, *Materials Letters* **62**, 2008, 1297-1301
- [19] Z. Gan, G. Ning, Y. Lin and Y. Cong, Morphological Control of Mesoporous Alumina Nanostructures via Template-Free Solvothermal Synthesis, *Materials Letters* **61**, 2007, 3758-3761
- [20] D. H. M. Buchold and C. Feldmann, Nanoscale γ -AlO(OH) Hollow Spheres: Synthesis and Container-Type Functionality, *Nano Letters* **7**, 2007, 3489-3492
- [21] S. C. Shen, Q. Chen, P. S. Chow, G. H. Tan, X. T. Zeng, Z. Wang and R. B. H. Tan, Steam-Assisted Solid Wet-Gel Synthesis of High-Quality Nanorods of Boehmite and Alumina, *Journal of Physical Chemistry C* **111**, 2007, 700-707
- [22] Y. P. Lee, Y. H. Liu and C. S. Yeh, Formation of Bayerite, Gibbsite and Boehmite Particles by Laser Ablation, *Physical Chemistry Chemical Physics* **1**, 1999, 4681-4686
- [23] H. S. Potdar, K. W. Jun, J. W. Bae, S. M. Kim and Y. J. Lee, Synthesis of Nanosized Porous γ -Alumina via a Precipitation/Digestion Route, *Applied Catalysis A: General* **321**, 2007, 109-116
- [24] M. Rajendran and A. K. Bhattacharya, Low-Temperature Formation of Alpha Alumina Powders from Carboxylate and Mixed Carboxylate Precursors, *Materials Letters* **39**, 1999, 188-195
- [25] T. Tsuchida and K. Kodaira, Hydrothermal Synthesis and Characterization of Diaspre, β -Al₂O₃·H₂O, *Journal of Materials Science* **25**, 1990, 4423-4426
- [26] J. Livage, Sol-Gel Synthesis of Heterogeneous Catalysts from Aqueous Solutions, *Catalysis Today* **41**, 1998, 3-19
- [27] H. L. Wen and F. S. Yen, Growth Characteristics of Boehmite-Derived Ultrafine Theta and Alpha-Alumina Particles During Phase Transformation, *Journal of Crystal Growth* **208**, 2000, 696-708
- [28] R. B. Bagwell and G. Messing, Effect of Seeding and Water Vapor on the Nucleation and Growth of α -Al₂O₃ from γ -Al₂O₃, *Journal of the American Ceramic Society* **82**, 1999, 825-832

- [29] M. Kumagai and G. L. Messing, Controlled Transformation and Sintering of A Boehmite Sol-Gel by α -Alumina Seeding, *Journal of the American Ceramic Society* **68**, 1985, 500-505
- [30] J. L. McArdle and G. L. Messing, Transformation, Microstructure Development, and Densification in α -Fe₂O₃ Seeded Boehmite Derived Alumina, *Journal of the American Ceramic Society* **76**, 1993, 214-222
- [31] R. A. Shelleman, G. L. Messing and M. Kumagai, Alpha Alumina Transformation in Seeded Boehmite Gels, *Journal of Non-Crystalline Solids* **82**, 1986, 277-285
- [32] R. B. Bagwell, G. L. Messing and P. R. Howell, The Formation of α -Alumina from θ -Alumina: The Relevance of a “Critical Size” and Diffusional Nucleation or “Synchro-Shear”, *Journal of Materials Science* **36**, 2001, 1833-1841
- [33] M. Kumagai and G. L. Messing, Enhanced Densification of Boehmite Sol Gels by Alpha Alumina Seeding, *Journal of the American Ceramic Society* **67**, 1984, c230-231
- [34] H. J. Kim, T. G. Kim, J. J. Kim, S. S. Park, S. S. Hong and G. D. Lee, Influences of Precursor and Additive on the Morphology of Nanocrystalline α -Alumina, *Journal of Physics and Chemistry of Solids* **69**, 2008, 1521-1524
- [35] H. Liu, G. Ning, Z. Gan and Y. Lin, Emulsion-Based Synthesis of Unaggregated, Spherical Alpha Alumina, *Material Letters* **62**, 2008, 1685-1688
- [36] S. G. Lee, H. C. Park, B. S. Kang, G. S. Seo, S. S. Hong and S. S. Park, Synthesis of α -Alumina Platelets from γ -Alumina with and without Microwaves, *Materials Science and Engineering A* **466**, 2007, 79-83
- [37] H. Gocmez and O. Özcan, Low Temperature Synthesis of Nanocrystalline α -Al₂O₃ by a Tartaric Acid Gel Method, *Materials Science and Engineering A* **475**, 2008, 20-22
- [38] J. Li, Y. Pan, C. Xiang, Q. Ge and J. Guo, Low Temperature Synthesis of Ultrafine α -Al₂O₃ Powder by a Simple Aqueous Sol-Gel Process, *Ceramics International* **32**, 2006, 587-591
- [39] R. M. Laine, J. C. Marchal, H. P. Sun and X. Q. Pan, Nano- α -Al₂O₃ by Liquid-Feed Flame Spray Pyrolysis, *Nature Materials* **5**, 2006, 710-712
- [40] P. K. Sharma, V. V. Varadan and V. K. Varadan, A Critical Role of pH in the Colloidal Synthesis and Phase Transformation of Nano Size α -Al₂O₃ with High Surface Area, *Journal of the European Ceramic Society* **23**, 2003, 659-666
- [41] Y. Q. Wu, Y. F. Zhang, X. X. Huang and J. K. Guo, Preparation of Platelike Nano Alpha Alumina Particles, *Ceramics International* **27**, 2001, 265-268
- [42] R. W. Jones, Fundamental Principles of Sol-Gel Technology, The Institute of Metals, London, 1989
- [43] M. Ebelmen, Sur les Combinaisons des Acides Borique et Silicique avec les Ethers, *Annales de Chimie et de Physique* **16**, 1846, 129

- [44] J. Livage, Sol-Gel Synthesis of Inorganic Materials, *Encyclopedia of Materials: Science and Technology* 2001, 4105-4107
- [45] D. Chen, Anti-Reflection (AR) Coatings Made by Sol-Gel Processes: a Review, *Solar Energy Materials & Solar Cells* **68**, 2001, 313-336
- [46] J. Wang, Sol-Gel Materials for Electrochemical Biosensors, *Analytica Chimica Acta* **399**, 1999, 21-27
- [47] H. K. Farag and F. Endres, Studies on the Synthesis of Nano-Alumina in Air and Water Stable Ionic Liquids, *Journal of Materials Chemistry* **18**, 2008, 442-449
- [48] E. J. Nassar, K. J. Ciuffi, R. R. Goncalves, Y. Messaddeg, and S. J. L. Ribeiro, Titanium-Silicon Films Prepared by Spin and Dip-Coating, *Química Nova* **26**, 2003, 754-756
- [49] K. Tadanaga, N. Katata and T. Minami, Super-Water-Repellent Al₂O₃ Coating Films with High Transpatency, *Journal of the American Ceramic Society* **80**, 1997, 1040-1042
- [50] K. Tadanaga, N. Katata and T. Minami, Formaiton Process of Super-Water-Repellent Al₂O₃ Coating Films with High Transpatency by the Sol-Gel Method, *Journal of the American Ceramic Society* **80**, 1997, 3213-3216
- [51] K. Tadanaga, K. Kitamuro, A. Matsuda and T. Minami, Formation of Superhydrophobic Alumina Coating with High Transprency on Polymer Substrate by the Sol-Gel Method, *Journal of Sol-Gel Science and Technology* **26**, 2003, 705-708
- [52] J. Genzer and A. Marmur, Biological and Synthetic Self-Cleaning Surfaces, *Materials Research Society Bulletin* **33**, 2008, 742-746
- [53] W. Barthlott and C. Neihuis, Purity of the Sacred Lotus, or Escape from Contamination in Biological Surfaces, *Planta* **202**, 1997, 1-8
- [54] K. Tadanaga, J. Morinaga, A. Matsuda and T. Minami, Superhydrophobic-Superhydrophilic Micropatterning on Flowerlike Alumina Coating Film by the Sol-Gel Method, *Chemistry of Materials* **12**, 2000, 590-592
- [55] M. Miwa, A. Nakajima, A. Fujishima, K. Hashimoti and T. Watanabe, Effects of the Surface Roughness on Sliding Angles of Water Droplets on Superhydrophobic Surfaces, *Langmuir* **16**, 2000, 5754-5760
- [56] R. N. Wenzel, Resistance of Solid Surfaces to Wetting by Water, *Industrial & Engineering Chemistry* **28**, 1936, 988-994
- [57] A. B. D Cassie and S. Baxter, Wettability of Porous Surfaces, *Transactions of the Faraday Society* **18**, 1944, 546-551
- [58] L. Feng, S. Li, Y. Li, H. Li, L. Zhang, J. Zhai, Y. Song, B. Liu, L. Jiang and D. Zhu, Super-Hydrophobic Surface: From Natural to Artificial, *Advanced Materials* **14**, 2002, 1857-1860

- [59] H. M. Shang, Y. Wang, S. J. Limmer, T. P. Chou, K. Takahashi and G. Z. Cao, Optically Transparent Superhydrophobic Silica-Based Films, *Thin Solid Films* **472**, 2005, 37-43
- [60] E. O. Zayim, Optical and Electrochromic Properties of Sol-Gel Made Anti-Reflective WO₃-TiO₂ Films, *Solar Energy Materials & Solar Cells* **87**, 2005, 695-703
- [61] P. Nostell, A. Roos and B. Karlsson, Optical and Mechanical Properties of Sol-Gel Antireflective Films for Solar Energy Applications, *Thin Solid Films* **351**, 1999, 170-175
- [62] G. S. Vicente, A. Morales and M. T. Gutierrez, Preparation and Characterization of Sol-Gel TiO₂ Antireflective Coatings for Silicon, *Thin Solid Films* **391**, 2001, 133-137
- [63] E. Hammarberg and A. Roos, Antireflective Treatment of Low-Emitting Glazings for Energy Windows with High Visible Transmittance, *Thin Solid Films* **442**, 2000, 222-226
- [64] T. Morimoto, Y. Sanada and H. Tomogana, Wet Chemical Functional Coatings for Automotive Glasses and Cathode Ray Tubes, *Thin Solid Films* **392**, 2001, 214-222
- [65] M. Lechna, I. Holowacz, A. Ulatowska and H. Podbielska, Optical Properties of Sol-Gel Coatings for Fiberoptic Sensors, *Surface and Coating Technology* **151&152**, 2002, 299-302
- [66] O. S. Heavens, Optical Properties of Thin Solid Films, Dover Publications Inc., New York, 1991
- [67] J. Hiller, J. D. Mendelsohn and M. F. Rubner, Reversibly Erasable Nanoporous Anti-Reflective Coatings from Polyelectrolyte Multilayers, *Nature Materials* **1**, 2002, 59-63
- [68] A. R. Parker, Natural Photonic Engineers, *Materials Today* **5**, 2002, 26-31
- [69] B. E. Yoldas, Investigation of Porous Oxides as an Antireflective Coating for Glass Surfaces, *Applied Optics* **19**, 1980, 1425-1429
- [70] Q. Xie, J. Xu, L. Feng, L. Jiang, W. Tang, X. Luo and C.C. Han, Facile Creation of a Super-Amphiphobic Coating Surface with Bionic Microstructure, *Advanced Materials* **16**, 2004, 302-305
- [71] J. Zhang, J. Li and Y. Han, Superhydrophobic FTFE Surfaces by Extension, *Macromolecular Rapid Communication* **25**, 2005, 1105-1108
- [72] H. Y. Erbil, A. L. Demirel, Y. Avci and O. Mert, Transformation of a Simple Plastic into a Superhydrophobic Surface, *Science* **299**, 2003, 1377-1380
- [73] X. Lu, C. Zhang and Y. Han, Low-Density Polyethylene Superhydrophobic Surface by Control of Its Crystallization Behavior, *Macromolecular Rapid Communication* **25**, 2004, 1606-1610

- [74] H. Li, X. Wang, Y. Song, Y. Liu, Q. Li, L. Jiang and D. Zhu, Super-Amphiphobic Aligned Carbon Nanotube Films, *Angewandte Chemie International Edition* **40**, 2001, 1743-1746
- [75] K. K. S. Lau, J. Bico, K. B. K. Teo, M. Chhowalla, G. A. J. Amaratunga, W. I. Milne, G. H. McKinley and K. K. Gleason, Superhydrophobic Carbon Nanotube Forests, *Nano Letters* **3**, 2003, 1701-1705
- [76] A. Nakajima, K. Hashimoto and T. Watanabe, Transparent Superhydrophobic Thin Films with Self-Cleaning Properties, *Langmuir* **16**, 2000, 7044-7047
- [77] A. Nakajima, A. Fujishima, Kazuhito and T. Watanabe, Preparation of Transparent Superhydrophobic Boehmite and Silica Films by Sublimation of Aluminum Acetylacetonate, *Advanced Materials* **11**, 1999, 1365-1368
- [78] B. Qian and Z. Shen, Fabrication of Superhydrophobic Surface by Dislocation-Selective Chemical Etching on Aluminum, Copper and Zinc Substrates, *Langmuir* **21**, 2005, 9007-9009
- [79] A. Hozumi and O. Takai, Preparation of Silicon Oxide Films Having a Water-Repellent Layer by Multiple-Step Microwave Plasma-Enhanced Chemical Vapor Deposition, *Thin Solid Films* **334**, 1998, 54-59
- [80] F. Rouquerol, J. Rouquerol and K. Sing, Adsorption by Powders and Porous Solids: Principles, Methodology and Applications, Academic Press, 1999
- [81] J. Peltonen, M. Järn, S. Areva, M. Linden and J. B. Rosenholm, Topographical Parameters for Specifying a Three-Dimensional Surface, *Langmuir* **20**, 2004, 9428-9431
- [82] H. Y. Zhu, J. D. Riches and J. C. Barry, γ -Alumina Nanofibers Prepared from Aluminum Hydrate with Poly(ethylene oxide) Surfactant, *Chemistry of Materials* **14**, 2002, 2086-2093
- [83] S. Lowell and J. E. Shields, Powder Surface Area and Porosity, 2nd edition, Chapman and Hall, 1984
- [84] C. Sangwichien, G. L. Aranovich and M. D. Donohue, Density Functional Theory Predictions of Adsorption Isotherms with Hysteresis Loops, *Colloids and Surfaces A: Physicochemical and Engineering Aspects* **206**, 2002, 313-320
- [85] S. Bhaduri, E. Zhou and S. B. Bhaduri, Auto Ignition Processing of Nanocrystalline α -Alumina, *Nanostructured Materials* **7**, 1996, 487-496
- [86] G. C. Bye and G. T. Simpkin, Influence of Cr and Fe on Formation of α -Alumina from γ -Alumina, *Journal of the American Ceramic Society* **76**, 1974, 367-371
- [87] J. R. Wynnycyk and C. G. Morris, A Shear-Type Allotropic Transformation in Alumina, *Metallurgical and Materials Transactions* **16B**, 1985, 345-353
- [88] P. Padmaja, P. K. Pillai, K. G. K. Warriar and M. Padmanabhan, Adsorption Isotherm and Pore Characteristics of Nano Alumina Derived from Sol-Gel Boehmite, *Journal of Porous Materials* **11**, 2004, 147-155

ABSTRACTS OF THE PUBLICATIONS I-VII

- I Flaky boehmite (γ -AlOOH) powder with a BET surface area of 303 m²/g was synthesized. The phase transformation upon heat-treatments from 500 to 1000 °C to transition alumina (γ -, δ -, θ -alumina) was studied by X-ray diffraction (XRD). The morphologies of nanoparticles and nanorods were revealed by transmission electron microscopy (TEM). The BET surface area, pore size distribution and pore structure of the different transition aluminas at different calcination temperatures were also studied by N₂ adsorption/desorption test. When calcined from 500 to 800 °C, γ -alumina nanoparticles and nanorods were formed with BET surface areas ranging from 438 to 200 m²/g. At 900 °C, δ - and γ -alumina coexisted with a BET surface area of 124 m²/g, showing morphologies of both nanoparticles and nanorods. At 1000 °C, the sample with morphology of only nanorods was a mixture of θ - and δ -alumina, possibly also γ -alumina with a BET surface area of 79 m²/g.
- II Nanocrystalline α -alumina powder with novel morphology has been synthesized at a relatively low temperature of 1000 °C without any seeding material, in which 5 nm-crystallites of α -alumina exist on the surface of the nanorods having widths of about 15 nm and lengths ranging from 50 to 300 nm.
- III We have reported in a short communication that nanocrystalline α -alumina powder with novel morphology was synthesized at a relatively low temperature of 1000 °C without any seed material. In this follow up full paper, detailed processing parameters of such nanocrystalline α -alumina are reported and more characterizations are carried out in order to study the mechanism of the synthesis. The formation scheme of the novel morphology of such nanocrystalline α -alumina is illustrated and the phase transformation from θ - to α -alumina is discussed.
- IV Nanocrystalline α -alumina powders in different morphology obtained from gel powder and boehmite (γ -AlOOH) powder are compared in this paper. The boehmite powder in flaky morphology was prepared by reacting the gel powder with boiling water. Spherical α -alumina was obtained by calcining the gel powder at 1000 °C for 6 h, while rod-shaped α -alumina with 5 nm-crystallites on the surface of the nanorods was synthesized by calcining the flaky boehmite powder at 1000 °C for 40 h. Phase transformation and morphology are characterized by X-ray diffraction (XRD), thermogravimetry-differential scanning calorimetry (TG-DSC) and transmission electron microscopy (TEM). The formation scheme of the different morphology is comparatively illustrated and furthermore the phase transformation to α -alumina is discussed.

- V The effect of heat-treating gel films at different temperatures on the formation of the flaky structure of boehmite on AISI 316 type austenitic stainless steel is investigated. After heating at different temperatures, the reactivity of the gel films with boiling water to form boehmite flakes was different, which resulted in different morphologies and different contact angle values after coating with hydrolyzed FAS. When the gel film was heat-treated from 200 to 600 °C, the resulting contact angles were above 150°, indicating the superhydrophobic behavior. However, when the gel film was heat-treated below 200 °C as well as at 700 and 800 °C, only some boehmite flakes were formed; when the gel film was heat-treated at 900 °C, flaky structure was not observed. In these cases the surface roughness is insufficient for the superhydrophobicity. The formation condition of the boehmite flakes by reaction of the gel film with boiling water is also tentatively discussed.
- VI Boehmite thin film with 50-100 nm flaky surface structure was synthesized on AISI 316 type austenitic stainless steel by immersing the gel film into boiling water. When further coated with hydrolyzed FAS, the surface became superhydrophobic with a contact angle for water of 152°. The superhydrophobic property resulted from both the nanoscale flaky surface structure and the low surface energy of the FAS top layer. The topography of such film was revealed by atomic force microscopy (AFM) and a set of roughness parameters of such film was obtained. The degradation of superhydrophobicity of the surface was studied as a function of the post heat-treatment temperatures. Below 600 °C, the surface remained to be superhydrophobic with the FAS top layer. Above 700 °C, the surface was not superhydrophobic any more due to a gradual loss in surface roughness which was revealed by field emission scanning electron microscopy (FESEM). The morphology change during the post heat-treatments from 700 to 900 °C was studied by transmission electron microscopy (TEM).
- VII Superhydrophobic antireflective boehmite films with different topographies were made by the sol-gel process with variation of pre heat-treatment temperatures and film thicknesses. A set of roughness parameters was determined from atomic force microscopy (AFM) to relate the superhydrophobic and antireflective properties to the surface topography. The results demonstrate the power of the roughness parameters to identify the superhydrophobic and antireflective properties.